Longitudinal dissection in brain organoids at single cell resolution uncovers the developmental role of GSK3 in human corticogenesis

Alejandro López-Tobón[1,2,*], Carlo Emanuele Villa[1,*], Cristina Cheroni[1,*], Sebastiano Trattaro[1], Nicolò Caporale[1], Paola Conforti[3], Raffaele Iennaco[3], Maria Lachgar[4,a], Marco Tullio Rigoli[1], Berta Marcó de la Cruz[1,], Pietro Lo Riso[1], Erika Tenderini[1], Flavia Troglio[1], Marco de Simone[5], Isabel Liste-Noya[4], Stefano Piccolo[6], Giuseppe Macino[7], Massimiliano Pagani[5,6], Elena Cattaneo[3] and Giuseppe Testa[1,2, *].

[1]Laboratory of Stem Cell Epigenetics, IEO, European Institute of Oncology, IRCCS, Milan, Italy Milan, Italy

[2]Department of Oncology and Hemato-oncology, Università degli studi di Milano, Milan, Italy

[3]Istituto Nazionale Genetica Molecolare, INGM, Milan Italy

[4]Unidad de Regeneración Neural, Unidad Funcional de Investigación de Enfermedades Crónicas, Instituto de Salud Carlos III (ISCIII), Madrid, Spain

[5]Istituto Nazionale Genetica Molecolare INGM 'Romeo ed Enrica Invernizzi', Milan 20122, Italy.

[6]Department of Medical Biotechnology and Translational Medicine, Università degli Studi di Milano, Milano

[7]Department of Cellular Biotechnologies and Hematology, La Sapienza University of Rome, Rome, Italy 20129, Italy.

[*]Co-first authors listed by order of joining the project

Current location:

[a] Servicio de Genética, Instituto Ramón y Cajal de Investigación Sanitaria, Hospital Universitario Ramón y Cajal, Madrid, Spain,

[*]correspondence to: giuseppe.testa@ieo.it or giuseppe.testa@unimi.it

Key words: human brain organoids, single cell, GSK3, corticogenesis

Summary

The regulation of proliferation and polarity of neural progenitors is crucial for the development of the brain cortex, with modes and timings of cell division intimately related to the stereotypical acquisition of layer-specific neuronal identities. Animal studies have implicated glycogen synthase kinase 3 (GSK3) as a pivotal regulator of both proliferation and polarity, yet the functional relevance of its signaling for the unique features of human corticogenesis remain to be elucidated. Here we harness human cortical brain organoids to probe, at single cell resolution, the longitudinal impact of GSK3 inhibition through multiple developmental stages. Our results indicate that chronic GSK3 inhibition increases the proliferation of neural progenitors and causes massive derangement of cortical tissue architecture. Surprisingly, single cell transcriptome profiling revealed only a discrete impact on early neurogenesis and uncovered the outer radial glia and the astrogenic lineage as the main GSK3-dependent developmental domains. Through this first single cell-level dissection of the GSK3 regulatory network in human corticogenesis, our work uncovers a remarkably specific conduit between the architecture of progenitor niches and lineage specification.

Introduction

The onset of neurogenesis is governed by two main processes: i) the formation of a neuroepithelium, composed by neural stem cells (NSCs) which display glial hallmarks and organize themselves in apico-basal orientation and ii) consecutive waves of symmetric divisions that lead to a rapid expansion of the NSC pool (Taverna et al., 2014). The polarization of NSCs allows to unambiguously confer a progenitor identity and precedes the elongation of cytoplasmic processes that form a migratory scaffold for newborn neurons (Betizeau et al., 2013). These polarization events are prerequisite for defining diverse NSC properties, in particular their proliferation capacity and stemness (Johansson et al., 2010; Lehtinen et al., 2011). The emergence of this organized structure results from the combination of cell autonomous genetic programs and their interaction with the context of the local 3-dimensional milieu, as morphogenic signals

may be conveyed via the ventricular fluid or the basal lamina, in gradients with a precise spatial distribution (Lehtinen et al., 2011).

Glycogen synthase kinase 3 (GSK3α and β) are serine/threonine kinases known to constitute an integrating hub for multiple proliferation and differentiation signals due to their central role in the receptor tyrosine kinase, Wnt and sonic hedgehog signaling pathways (Harrison-Uy and Pleasure, 2012; McCubrey et al., 2016). GSK3 mediate control on neurodevelopment through the regulation of a broad set of substrates, including transcription factors essential for brain development, such as CREB (Grimes and Jope, 2001a), neurogenin2 (Ma et al., 2008), β-catenin (Aberle et al., 1997), microtubule-associated proteins required for the organization of the mitotic spindle during the cell cycle (Fumoto et al., 2008) and cytoskeletal dynamics in growth cones during axon development (Zhou et al., 2004). Studies in animal models have rendered a wealth of evidence indicating that GSK3 activity is pivotal to the regulation of early and late neurogenesis in a stage-wise fashion. Indeed, its regulation is required to maintain the overall polarity of the radial glia scaffold (Yokota et al., 2010). The ablation of GSK3β leads to enlarged neuroepithelium and lateral ventricles, as a result of cell cycle reentry and increased progenitor proliferation (Chenn and Walsh, 2003), which is consistent with its reported role in regulating the stability and function of β-catenin (Kim et al., 2009). Depletion of either GSK3α or GSK3β promotes the proliferation of neural progenitor cells in the ventricular zone, but at later stages, the knockdown of each isoform results in distinct outcomes. GSK3β in particular controls the transformation of radial progenitors to intermediate progenitor cells in a GSK3α-independent fashion (Ma et al., 2017). Moreover, knocking down GSK3β but not GSK3α prevents the generation of upper-layer Cux1 neurons. Consistent with these distinct outcomes, protein levels of c-Myc and β-catenin, well-known substrates of GSK3, are differentially affected by depletion of GSK3α and GSK3β (Ma et al., 2017).

Activation of Wnt signaling as a result of GSK3 inhibition has been implicated both in neuroepithelial and apical radial glial cell expansion as well as in differentiation of basal progenitors, with the final outcome largely depending on the signaling context (Harrison-Uy and Pleasure, 2012). The activation of the Wnt leads to the accumulation of free β-catenin and its translocation to the nucleus, where it regulates proliferation and differentiation genes (Holland et al., 2013). Canonical Wnt pathway is active in cortical progenitor cells during early forebrain development in a high-medial to low-lateral pattern and as development progresses, cortical Wnt signaling decreases (Backman et al., 2005). Later on, the Wnt-rich cortical hem controls the development of adjacent cortical structures, such as the hippocampus and choroid plexus. Likewise, the inhibition of GSK3 during neural induction of mouse pluripotent stem cells, results in the generation of neural progenitors of different rostro-caudal identity in a dose-dependent manner, whereas higher levels of inhibitor induce cells with more caudal identity, such as the midbrain (Hirabayashi et al., 2004; Kuwahara et al., 2010).

Despite the abundant evidence connecting GSK3 to neurogenesis in various animal models, much less is known of its role in the far more complex human context, mostly due to the lack of models that efficiently recapitulate its wealth of progenitor subpopulations. Seminal work conducted in human embryonic stem cells (hESCs) demonstrated their proficiency to form 3-dimensional aggregates containing self-organized apico-basally polarized cortical tissues with neurogenic properties (Watanabe et al., 2005). These 3-dimensional aggregates are able to generate features usually absent in monolayer cultures such as specific progenitor subpopulations and organizing centers (Eiraku et al., 2008; Kadoshima et al., 2013), constituting the precursors of current brain organoids protocols. Brain organoids have emerged as the most promising alternative to study neurodevelopment under a strictly human genetic background (Di Lullo and Kriegstein, 2017). Their ontogeny recapitulates all the main aspects of early to mid brain development, including progenitor populations and distribution of cell domains (Lancaster et al., 2013; Paşca et al., 2015a). Strikingly, brain organoids show transcriptional and epigenetic signatures, such as global patterns of non-CG methylation, unique to the human cortical development (Luo et al., 2016). Single cell transcriptional

profiling of organoids revealed a cellular diversity that closely matches in composition and transcriptional landscape the human fetal brain and confirmed the presence of human progenitor populations responsible for neocortical expansion (Camp et al., 2015; Quadrato et al., 2017). More recently, the integration of multiple patterned organoids, or "assembloids", has allowed the combination of brain subdomains proving groundbreaking for studying interneuron migration and circuit integration (Bagley et al., 2017; Birey et al., 2017).

Here we explore the effect of the chronic inhibition of GSK3 during corticogenesis from early neural induction to middle corticogenesis in human cortical organoids. By combining morphological characterization with massive parallel RNA sequencing on bulk and single cells, we uncover the gene sets modulated by GSK3 and breakdown their impact on distinct cell subpopulations of the developing human cortex, revealing a differential regulation of direct and protracted neurogenic trajectories by GSK3 activity.

Materials and Methods

hPSC culture. hPSC lines were cultured under feeder-free conditions on Matrigel (BD Biosciences) coated dishes (diluted 1:40 matrigel:DMEM/F12) and grown in Tesr™ E8™ medium (Stem Cell Technologies). Cells were passaged upon treatment with ReLeSR (Stem Cell Technologies). All differentiation procedures were performed on iPSC lines with at least 15 passages after reprogramming. Pluripotent lines came from different individuals representing either human iPSC or ESC lines previously described (Adamo et al., 2015; González et al., 2014). All the cultures are regularly tested and maintained mycoplasma free. The distribution of lines across experiments is delineated in Supplementary table 1.

Neural induction in 2D and lumen quantification. Briefly, hPSC cells were plated at a density of 0.7 × 10^5 cells cm^2 on Matrigel (BD Biosciences) coated dishes in grow medium supplemented with 10 µM ROCK inhibitor (Y-2763221, Cell Guidance System). Cell cultures were expanded for two days until they were 70% confluent. The starting differentiation medium includes DMEM/F12 (Life Technologies) with

N2 and B27 without retinoic acid (Life Technologies), supplemented with 500 nM LDN193189 (Sigma) and 10 µM SB431542 (Tocris). From day 0 CHIR99021 was added to the medium at 1 µM concentration in parallel with neural induction without CHIR99021 until day 20. At day 12 cells were moved to neural medium containing DMEM/F12 (Life Technologies) with N2 and B27 plus retinoic acid and 30ng ml-1 BDNF. For lumen quantification cells were fixed at day 20 in 4% (wt/vol) paraformaldehyde (PFA) for 15 minutes at room temperature (RT) and washed 3 times with phosphate-buffered saline (PBS). Cells were then permeabilized with PBS containing 0.5% Triton X-100 (Sigma) and blocked with 10% (vol/vol) normal goat serum (NGS; Vector) for 1 hour at RT. Next, cells were incubated overnight at 4°C. The following primary antibodies and dilutions were used: anti-Ncadherin, 1:800 (BD Biosciences) and anti-PALS1, 1:500 (Cell Signaling Technology). Object identification module of Cell Profiler software (v.2.1.1) was used to automatically quantify lumens (number and size of Pals1 positive areas) of neural rosettes.

Proliferation assay. Number of viable proliferating cells was estimated by luminiscence assay CellTiter-Glo® (Promega). Briefly, $2x10^3$ cells/well were plated in 96-well flat bottom plates (Corning) with 4 replicates per condition and left to proliferate for 96 hours. Measurements were performed every 24 hours. Each data point was normalized to a blank from unseeded wells.

Cortical Organoid differentiation and inhibition. Cortical organoids were differentiated as previously described (Paşca et al., 2015). hPSCs were plated onto cell cycle-arrested mouse embryonic feeders (MEFs)(Millipore) for one passage, colonies grown for at least 48h and then enzymatically detached by incubation with 0.7 mg/ml dispase (Invitrogen: 17105-041) for approx. 30 min. Suspended colonies were subsequently transferred into ultra-low-attachment 100 mm plastic plates (Corning) in FGF2-free knockout serum medium. For the first 24 h (day 0), the medium was supplemented with the ROCK inhibitor Y-27632 (EMD Chemicals). For neural induction, dorsomorphin (Merck, 5 µM) and SB-431542 (Tocris, 10 µM) were added to the medium until day 5. From day 6 onward, organoids were moved to neural medium (NM) containing Neurobasal (Invitrogen 10888), B-27 serum substitute without vitamin A (Invitrogen 12587),

GlutaMax 1:100 (Fisher 35050071), 100 U/ml penicillin and streptomycin (Invitrogen) and 50 mM b-Mercaptoethanol (Gibco 31350010). The NM was supplemented with 20 ng/ml FGF2 (Thermo) and 20 ng/ml EGF (Tocris) for 19 days with daily medium change in the first 10 days, and every other day for the subsequent 9 days. On day 12, floating organoids were moved to orbital shaker (VWR Standard Orbital Shaker, Model 1000) and kept on constant shaking at 50 rpm to promote nutrient and oxygen exchange. To induce neurogenesis, FGF2 and EGF were replaced with 20 ng/ml BDNF (Peprotech) and 20 ng/ml NT3 (Peprotech) starting at day 25, while from day 43 onwards only NM without growth factors was used for medium changes every other day. Chronic GSK3 inhibition was performed by adding CHIR99021 (Merck SML1046) to the medium at day 0 (1 μM) and kept throughout the differentiation process until reaching the respective sample collection timepoints.

Growth curve. Organoids were moved at day 0 to 96-well U-bottom ultra-low attachment plates (Corning) and kept individually in order to avoid fusions for image acquisition until day 12 of differentiation. From day 12 onwards, organoids were moved individually to 24-well ultra-low attachment plates (Corning). Images were acquired with an EVOS Cell imaging System XL (Thermo) at the indicated differentiation days. Organoid size was calculated using an in-house developed a custom-script (by CEV) for FIJI software (v.1.49 NIH-USA).

Tissue preservation and staining. Organoids were fixed in 4% (vol/vol) paraformaldehyde (PFA) for a minimum of 2h for day 18 organoids to overnight for day 50. Fixed organoids were washed twice with PBS and mounted on OCT cryopreservation medium on dry ice. Cryoblocks were preserved at -80 ^{o}C until the moment of sectioning. Cryosections were prepared using Leica CM 1900 instrument with 5 μm thickness. Sections were incubated with 10 mM Sodium citrate buffer (Normapur) for 45 min at 95°C + Tween 20 0,5% for simultaneous antigen retrieval and permeabilization. Primary antibodies were prepared in PBS + 5% normal donkey serum (Jackson Immuno Resarch) overnight at 4°C. The following primary antibodies and dilutions were used: anti-PAX6, 1:200 (Biolegend); anti-KI67, 1:200 (Abcam 15580); anti-NESTIN, 1:500 (Millipore); anti–DCX, 1:1000 (BD Biosciences 611706); anti-TBR1, 1:200 (Abcam 31940). After

primary incubation, sections were washed three times with PBS and the incubated with appropriate secondary antibodies conjugated to Alexa fluorophores 488 or 594 (Molecular Probes, Invitrogen) diluted 1:500 in blocking solution and incubated for 2 h at RT. Before mounting, sections were incubated with Hoechst 33258 (5 μg/mL; Molecular Probes, Invitrogen) or DAPI 1:5000 (Merck), as indicated on each caption. Images were acquired with a Leica DMI 6000B microscope (5×, 10×, and 20× objectives) and analyzed with LAS-AF imaging software and then processed using Image J (v1.49 NIH, USA) to adjust contrast for optimal RGB rendering. Confocal images were acquired with Leica SP8 microscope in resonant mode with Fluotar VISIR 25x/0.95 WATER objective, multiple tiles were acquired with PMT sensor and reconstructed via LASX software.

Total RNA extraction and sequencing. Total RNA was isolated with the RNeasy Micro Kit (Qiagen, Hilden, Germany) according to the manufacturer's instructions. RNA was quantified with Nanodrop and then the integrity was evaluated with Agilent 2100 Bioanalyzer (only if the quality ratios were not optimal after Nanodrop analysis). TruSeq Stranded Total RNA LT Sample Prep Kit, Illumina was used to run the library for each sample using 500 ng of total RNA as starting material. Sequencing was performed with the Illumina NOVAseq 6000 platform, sequencing on average 35 million 50bp paired-end reads per sample.

Bulk Transcriptome analysis. *Differential expression analysis.* Three biological replicates were analyzed for untreated and treated organoids at each time point, for a total of 18 samples subjected to bulk RNA sequencing. Gene expression quantification at the gene level was performed by Salmon (version 0.8.2)(Patro et al., 2017), using hg38 RefSeq annotation. To estimate differential expression, the matrix of gene counts was analyzed by edgeR (version 3.20.9) (Robinson et al., 2009). For each time point, genes with an expression level of at least 2 cpm (count per million) in at least 3 samples were selected for the analysis. Small genes, ribosomal genes and fusion genes were excluded. After TMM normalization, differential expression analysis comparing treated to untreated samples was performed using a likelihood ratio test on the coefficients of a negative binomial model. Significantly modulated genes were selected

setting an absolute value of log2 fold change (Log2FC) higher than 1 and a false discovery rate (FDR) lower than 5%. Log2 cpm values, calculated as implemented by edgeR, were used for heatmap representation of gene expression profiles (visualized as z-scores). Heatmaps were produced with pheatmap R package (version 1.0.10, Raivo Kolde (2018). pheatmap: Pretty Heatmaps.). Analyses were performed in R version 3.4.4.

Gene Ontology Enrichment Analysis. Gene ontology enrichment analysis for the Cellular Component domain of the ontology was performed on the 898 DEGs identified at day 50, splitted in up-regulated and down-regulated genes. The pool of tested genes (as selected for differential expression analysis) was used as background. The analysis was performed by TopGO ((version 2.30.1) (Adrian Alexa and Jorg Rahnenfuhrer 2016). topGO: Enrichment Analysis for Gene Ontology), relying on Fisher test and Weight01 method to take into account ontology hierarchy; minimum node size was set at 15. After imposing an enrichment cut-off of 2, a 0.01 p-value cut off was applied to select significantly enriched GO terms. Barplot in supplementary figure 4 shows the top-10 categories ranked for p-value.

Gene set enrichment analysis. GSEA was applied to each developmental stage with GSAA software, version 1.2 (Xiong et al., 2014). Raw reads for the same genes tested for differential expression were analyzed by GSAASeqSP (permutation type 'gene set'). H1 collection from the Molecular Signature Database was used as gene set source (Liberzon et al., 2015).

Single-Cell suspension, cDNA synthesis, library preparation and sequencing. Organoids were collected at day 50 or 100. 3-5 organoids per condition were dissociated by incubation with a solution of 0.5 mg/ml trypsin + 0,22 mg/ml EDTA (Euroclone) with 10 µl of DNaseI 1000 U/ml (Zymo Research) for 30 - 45 min according to organoid size. Digested suspensions were passed once through 0.4 µm Flowmi™ cell strainers, resuspended in PBS and counted using TC20 automatic cell counter (Biorad). Droplet-based single-cell partitioning and single-cell RNA-Seq libraries were generated using the Chromium Single-Cell 3′ Reagent v2 Kit (10× Genomics, Pleasanton, CA) following manufacturer's instructions (Zheng et al., 2017). Briefly, a small volume (6 - 8 µl) of single-cell suspension at a density of 1000 cells/µl was mixed

with RT-PCR master mix and immediately loaded together with Single-Cell 3′ gel beads and partitioning oil into a single-cell 3′ Chip. The gel beads were coated with unique primers bearing 10× cell barcodes, unique molecular identifiers (UMI) and poly(dT) sequences. The chip was then loaded onto a Chromium instrument (10× Genomics) for single-cell GEM generation and barcoding. RNA transcripts from single cells were reverse-transcribed within droplets to generate barcoded full-length cDNA using Clontech SMART technology. After emulsion disruption, cDNA molecules from one sample were pooled and preamplified. Finally, amplified cDNAs were fragmented, and adapter and sample indices were incorporated into finished libraries which were compatible with Illumina sequencing. The final libraries were quantified by Qubit system (Thermo) and calibrated with an in-house control sequencing library. The size profiles of the pre-amplified cDNA and sequencing libraries were examined by Agilent Bioanalyzer 2100 using a High Sensitivity DNA chip (Agilent). Two indexed libraries were equimolarly pooled and sequenced on Illumina NOVAseq 6000 platform using the v2 Kit (Illumina, San Diego, CA) with a customized paired-end, dual indexing format according to the recommendation by 10× Genomics. Using proper cluster density, a coverage around 250 M reads per sample (2000–5000 cells) were obtained corresponding to at least 50,000 reads/cell.

Single-Cell transcriptome analysis. Eleven biological samples (day 50: 3 untreated and 2 treated; day 100: 4 untreated and 2 treated) were examined by single cell analysis, for a total of 33293 cells and a median of 1733 features for cell. Libraries from single cell sequencing were aligned relying on the CellRanger v2.1 pipeline and using hg38 as reference. Before downstream analyses, data deriving from the 11 biological samples was integrated by Seurat v3.0-alpha analytical framework (Stuart et al., 2018). After normalization, anchors for data integration were identified considering 3000 anchor points (genes) and 40 dimensions. For data reduction, UMAP was applied with 50 nearest neighbors (nn); cluster initial positions were set considering PAGA node position (Scanpy v1.3.1) (Wolf et al., 2018). On the integrated dataset, clusters were identified by applying Louvain with Multilevel Refinement from Seurat with resolution parameter at 0.7. This resulted in the identification of 15 clusters. To characterize the clusters from a biological point of

view, we applied for each of them the FindMarker Seurat function, using MAST as test and filtering for up-regulated genes with fold change > 1.5 and adjusted P value < 0.05. The obtained lists were compared in a correlation analysis with gene lists deriving from a fetal single cell dataset (https://cells.ucsc.edu/?ds=cortex-dev) filtered with the same criteria. For the clusters of interest, cluster-wise differential expression analysis comparing treated to untreated cells at day 100 was performed using the FindMarker Seurat function, with MAST as test and filtering for adjusted P value < 0.05. Cluster-specific expression levels of biologically-relevant genes identified among the top dysregulated were visualized by violin plots, stratified for stage and treatment. Cell cycle analysis were performed using Scanpy function score_genes_cell_cycle, relying on the genes from (Kowalczyk et al., 2015)**.** Diffusion map algorithm for dimensionality reduction was performed with Scanpy with 50 nn. Pseudotime analysis for lineage branching reconstruction was applied using wishbone algorithm (Setty et al., 2016). The origin was defined as the cell showing the highest levels of the proliferation marker MKI67. The analysis was performed on the complete dataset, as well as separately for each of the four biological conditions in order to infer stage or treatment-selective trajectories; the origin was identified with the same method applied on complete dataset. RNA Velocity analysis was performed starting from the aligned (bam) files on one sample for each of the four biological conditions. Analysis was performed with the Velocyto algorithm, with mask for expressed repetitive elements downloaded from UCSC genome browser and the resulting loom file imported in python and analized with Scvelo https://github.com/theislab/scvelo. Partition-based graph abstraction (PAGA) algorithm was applied on the complete dataset, as well as separately for each of the four biological conditions and plotted with layout Reingold Tilford. The position of the nodes identified on the complete dataset was exploited in the graph for each biological condition.

Statistical Analysis. Statistical analyses were done using PRISM (GraphPad, version 6.0). Statistical significance was tested with the unpaired t-test, considering each line control line as biological replicates and comparing treatments as variables. N, p-values and significance are reported in each figure and legend. All results were expressed as means ± SD. No data points were excluded from the reported analyses.

Results

GSK3 is essential for cortical organoid morphogenesis

Patterned cortical organoids develop following a stereotypical morphogenesis beginning with NSCs radially aligned in 3-dimesions around ventricle-like structures (VLS), which resemble the ventricular zone of the developing telencephalon. Polarized NSCs are evident already prior to day 18 (Supp Fig 1), and by day18 NESTIN+/PAX6 + cells comprise about 80% of the population. This proportion decreases over time and becomes restricted to well-confined proliferative domains that gradually generate the neurons of the cortical plate (Paşca et al., 2015). In order to investigate the role of GSK3 activity throughout corticogenesis, we chronically exposed cortical organoids to the most specific GSK3 inhibitor available CHIR99021 (termed CHIR hereafter) at a concentration previously determined to affect specifically neurogenic properties, without inducing endo or mesodermal fates in hPSCs (Patsch et al., 2015). Such chronic GSK3 inhibition resulted in an increase in organoid size already evident by day 15 (Fig 1A, Fig 3A and Supp. Fig. 1A) concomitant with a virtually complete loss of VLS formation (Fig 1A-B), an effect that became even more dramatic by day 50 (Fig. 1C). Unexpectedly, this difference in organoid size and radial organization was accompanied by only a marginal decrease of PAX6+ cells at day 18 (CTL 76 ± 3.3, CHIR 65 ± 2.7) (as well as of its expression levels, Supp Fig. 3A), while no significant difference was observed at day 50 either in the proportion of PAX6+ cells (CTL 20 ± 1.2 N=14, CHIR 22 ± 1.0) or in its expression levels (as assessed by RNAseq). Moreover, staining for TBR1 (marker for layer V-VI neuronal progenitors) revealed a similar disarray in terms of tissue architecture, with only a slight reduction in TBR1+ cells upon GSK3 inhibition (CTL 39 ± 1.3, CHIR 32 ± 1.3), and no evident effect on the global levels of the early neuronal maturity marker doublecortin (DCX) (Supp. Fig. 2A-C, Fig. 3D), suggesting that GSK3 activity is not essential for accomplishing early neurogenesis. Taken together, these findings uncover a striking morphological disorganization in developing organoids induced by GSK3 inhibition, without a compelling change in the number of cells expressing markers of early neural maturity.

GSK3 inhibition disrupts organization and increases proliferation of neural stem cells

To dissect the mechanisms underlying this morphogenic defect, we adopted a two-tiered strategy. i) a validation in a classic 2D model attuned to quantify essential properties of neural stem cells such as polarity and proliferation (Conforti et al., 2018). ii) transcriptional profiling of patterned cortical organoids at 50 and 100days for a high-resolution dynamic characterization of early corticogenesis (Paşca et al., 2015) (Fig. 2A). First, we followed the emergence of 2D neural rosettes until 20 days *in vitro*, when rosettes are typically PASL1+ at the apical end. The quantification of rosette lumen area and size showed that GSK3 inhibition drastically reduces rosette number (Fig 2B,C) (CTL 6.8e-005 ± 4.3e-006, CHIR 2.1e-005 ± 3.5e-006) and likewise decreases the average size of formed rosettes (Fig 2D). In addition, quantification of the population growth at the first 72 hours post dual-smad inhibition shows an increase in proliferation rate up to 1.5-fold already after 72 hours (Fig 2E), suggesting that GSK3 activity is required to control proliferation rate and apico-basal organization during the transition from pluripotency to NSCs, providing a 2D correlate for both the disarray and the increased growth observed in early stage cortical organoids

Increased GSK3-dependent progenitor proliferation has a mild impact on early neurogenesis

Organoids typically reach a size limit probably caused by lack of vasculature, impairing proper oxygen and nutrient exchange and causing apoptosis of their core over time (Lancaster et al., 2013; McMurtrey, 2016). A previous report suggested that the sustained application of CHIR99021 in a patterned organoid protocol starting at day 12 of differentiation decreased the number of Caspase 3 + core cells (Qian et al., 2016). We tested whether the chronic CHIR application had an overall baseline effect on cell viability or increased the susceptibility of death after 72 hours of growth factor starvation. Luminescent quantitation of membrane permeability showed no changes in either base line (0 h) or susceptibility to cell death after 72 h of supplement starvation as a result of GSK3 inhibition (Fig 3A,B). Likewise staining for cleaved CAS3 showed no obvious differences (data not shown), suggesting that chronic GSK3 has no impact on basal or starvation-mediated cell death, nor is the increased organoid size a result of reduced apoptosis.

A growth curve of cortical organoids for 40 days of differentiation revealed instead a sustained increase in organoid size upon chronic GSK3 inhibition that picks up in pace between days 10 and 15, subsequent to the time point when cortical organoids begin to be exposed to proliferation boosting factors FGF2 and EGF (Fig 3A). This is in agreement with the increased proliferation rate observed at the first 72 hours of neural induction after dual-smad inhibition (Fig. 2E), and with the fact that CHIR exposure results in increased iPSCs proliferation even before neural induction (Esfandiari et al., 2012). However, although quantification of the active proliferation marker KI67 showed a sustained increase of actively proliferating cells in organoids at day 18 (CTL 10 ± 0.7, CHIR 19 ± 1.3) (Fig 2B, 3D) and day 50 (CTL 4.3 ± 0.4, CHIR 8.0 ± 0.8) (Fig 3C, E) no change in doublecortin levels was observed in day50 organoids (Fig 3D), pointing to the regulation of proliferation as a core aspect of GSKβ function that however does not significantly affect early neurogenesis.

Transcriptional regulation associated to GSK3 activity throughout cortical development

There is abundant evidence supporting an active role of GSK3 in neurogenesis (Hur and Zhou, 2010). However, since GSK3 ablation causes systemic failure and early embryonic lethality (Hoeflich et al., 2000), its levels/activity are usually manipulated both *in vitro* and *in vivo* after the early stages of neurodevelopment have already been completed. Against such expectations, the surprisingly mild effect of chronic GSK3 inhibition in neural maturation prompted us to dissect its role in gene expression at defining developmental points. Specifically, we assessed the impact of GSK3 inhibition on global gene expression by bulk RNAseq at three critical timepoints recapitulating relevant stages of human cortical development (i.e. day 18: highly abundant apical radial glia, day 50: presence of intermediate and early low layer neural progenitors and day 100: presence of middle- and upper-layer neural progenitors) (Paşca et al., 2015).

Principal component analysis (PCA) clearly indicated the stage of differentiation as the main source of variability and revealed an apparent delay of CHIR treated organoids throughout the differentiation process, an effect that was particularly obvious at day 50 (Fig. 4A). The second principal component (PC2) captured

instead the effect of CHIR treatment, which is likewise magnified at day 50 (Fig. 4A). By analyzing gene signatures defining specific stages of differentiation (high proliferation, neural induction and neuronal maturation), we confirmed the increase in expression of the proliferation marker MKI67 at all stages (Supp. Fig 3A-C), along with a differential impact on genes controlling distinct aspects of cell cycle progression, with a particularly strong upregulation at both day 50 and day 100 of the anaphase promoting complex/cyclosome (APC/C), CDC20 (Supp. Fig 3B,C). This protein has been implied in the modulating NEUROD2 levels through regulation of its ubiquitinization (Yang et al., 2009), thus favoring the determination and maintenance of neuronal fates.

Consistent with the immunohistochemical characterization (Fig 3D), the expression levels of neuronal maturity determinants confirmed no clear maturation imbalance, but rather a differential modulation of maturity markers in each condition (Supp. Fig 3 B,C), highlighted by a contrasting upregulation of TUBB3 and downregulation MAP2 in CHIR treated organoids, with no differences in doublecortin (DCX) levels. Interestingly, the analysis of transcriptional modulators of the glutamatergic lineage showed a strong downregulation of NEUROD2 at late stages (Supp. Fig 3 B,C), in line with its upstream downregulation by CDC20, which in turn may result at late stages in the observed differential modulation of several AMPA and NMDA receptor subunits (Telley et al., 2016) (Supp. Fig 3 B,C).

In order to address the functional implications of chronic CHIR exposure, we performed stage-wise differential expression analysis (DEA, Fig 4, B-D). DEA confirmed the amplification of CHIR effect at day 50, with a massive increase of differentially expressed genes (DEGs) (Fig 4 C) (full list of DEGs, supplementary table 2). Gene Ontology analysis revealed a persistent up-regulation of categories linked to cell proliferation and DNA replication (nucleosome assembly) and a down-regulation of cell surface components, as well as ion channels, including AMPA receptors (Supp. Fig 4 A-C). By overlapping DEGs across stages, we identified the gene sets that are consistently modulated throughout development (Fig 4, E-G). The overall comparison of gene modulation across stages showed a preserved trend, which was surprisingly stronger between d50->d100 compared to d18->d50, despite the longer timespan (Fig 4 F,G),

suggesting a more robust dependency of GSK3 activity occurring during this transition. While there were no genes dsyregulated throughout the entire differentiation process (ie. differentially regulated upon CHIR treatment at all three stages, day18, day50 and day100), we identified 9 DEGs consistently dysregulated in the d18->d50 transition and 54 DEGs between day50->day100. Functional breakdown shows that several d18->d50 shared down regulated genes are linked to neuritogenesis, as in the case of *RAB13, PTCHD1, NCL*, while at d50->d100 to axon development, as in the case of *ANKRD1*.

To gain deeper insight into the biological meaning of the coordinated modulation of functionally-related genes induced by GSK3 inhibition, we performed GSEA by Gene Set Association Analysis (GSAA). This approach confirmed a robust enrichment associated with CHIR treatment for pathways linked to GSK3 activity (MTORC1, Myc signalling) and furthermore narrowed down the upregulation of G2-M transition modulators as a persistent feature of GSK3 transcriptional impact at all stages (Fig 4H-J). Likewise, several of the identified GSEA categories (complete list in Supp. table 3) are directly linked to the observed phenotypes, including the increased progenitor production (mTORC1 pathway), changes of cell polarity (mitotic spindle orientation) and mixed neuronal fate (Wnt - β-Catenin pathway). Interestingly, both GO analysis at day 50 and GSEA (at all stages) point to the downregulation of inflammatory pathways by GSK3 inhibition, which is line with a recognized role of GSK3 as mediator of neuroinflammation (Grimes and Jope, 2001b).

Cortical organoids recapitulate the main features of mid-fetal human corticogenesis at the single cell level

Given the observation that the transcriptional impact of GSK3 inhibition peaked at day 50 and declined through day 100, we harnessed single cell transcriptomics combined with distance-based analytical tools to break-down the effects of CHIR exposure in terms of the trajectories followed by specific cell subpopulations during this developmental transition. We carried out droplet-based single-cell mRNA sequencing to profile over 30000 cells (N =33293) in 11 biological samples from unexposed and exposed cortical organoids at day 50 and day 100 of differentiation. Projection of the expression levels of canonical

population markers over Uniform Manifold Approximation and Projection (UMAP), an alternative to t-Distributed Stochastic Neighbor Embedding (tSNE) that enables the identification of clusters with an improved preservation of distance relationships (Betch et al., 2018), allowed us to pinpoint major developmental areas corresponding to early neurons (*DCX, ENO*), postmitotic neurons (*STMN2*) versus actively proliferating progenitors (*CDC20, MKI67*) (Fig 5A), bridged by areas rich in intermediate progenitors (*SB100*), outer radial glia (oRG) (*HOPX-FAM107A*) and early astrogenic progenitors (*CXCL14*) (Fig 5A). We next applied the Louven modularity algorithm (Šubelj and Bajec, 2011), a method developed for the extraction of communities from large networks, uncovering 15 unsupervised clusters that we associated to five main population identities (apical progenitors, astrogenic lineage, intermediate progenitors, early neurons and mature neurons) by interrogating human fetal single cell datasets (Nowakowski et al., 2017). (Fig 5B, Supp. Fig 5). Having defined this unbiased map of clusters, we could then investigate their underlying developmental trajectories, for which we used the diffusion map algorithm for dimensionality reduction to maintain the underlying structure of the original dataset and thereby preserve the directionality of cells' progression along developmental trajectories (Coifman et al., 2005) (Fig 5 C,D). Diffusion map uncovered the expected existence of one main developmental trajectory connecting proliferative progenitors to mature neurons through intermediate populations (Fig 5C). The application of pseudotime for lineage branching reconstruction (Haghverdi et al., 2016; Setty et al., 2016), with an origin anchored in the proliferation compartment by the highest level of MKI67 expression, confirmed this finding through the unbiased determination of the directional trajectory towards maturation (Fig 5D) and was further corroborated by the application of *RNA velocity* (La Manno et al., 2018), which infers the future transcriptional state of individual cells through the derivative of spliced-unspliced RNA abundances (Fig 5E). Likewise, the reconstruction of trajectories anchored on specific population markers validated the same findings, recapitulating a lineage path from early proliferative compartments through the intermediate progenitor-oRG transition and into early and late neural maturation stages (Fig 5F; MKI67 and CDK1 for proliferation; SMOC1 for intermediate progenitors; HOPX for oRG; DCX and STMN2 for maturity). Together, these results confirm that the longitudinal single cell analysis of patterned cortical organoids

between day 50 and 100 resolves the cardinal features of human corticogenesis including, importantly, the emergence of oRG and its central position in the secondary wave of neurogenesis

GSK3 inhibition differentially affects specific areas of corticogenesis.

A comparative analysis of the subpopulations identified above revealed the selective impact of GSK3 inhibition on the relative proportion of specific cell subtypes between controls and CHIR treated organoids (Fig 6A). The most outstanding effect was the complete absence, in CHIR-treated organoids, of a specific subset of cells from the astrogenic cluster, differentially characterized by the expression of (*CXCL14, HTR2C, TPD52L1*) (Fig 6B), along with several markers of the astrocytic lineage (Fig 5B). The other most affected areas revealed cluster-wise differential expression in key genes influencing fate specification in clusters of the maturity (cluster 0) (*GRIA2, MAP2, BCL11A, PCDH9*), intermediate (clusters 4,7) (*HES1, FABP5, HOPX, MT3, SPARCL1*), and astrogenic (cluster 11)(*CRIAB, PCP4, IGFBP5, TTR*) lineages (Supp. Fig 7). Interestingly, the analysis of cell population distribution across pseudotime (Fig 6C) uncovered an initially counterintuitive outcome featuring, at day 50, a higher proportion of cells in both proliferative and mature areas upon chronic GSK3 inhibition. This seemingly paradoxical result was compatible with two hypotheses: i) the cells identified as mature by predefined gene signatures could actually turn out to display mixed identities, co-expressing both progenitor and maturation markers as a result of a fundamental derangement of developmental order; or: ii) the highly proliferative progenitors from CHIR-treated organoids could transition faster through the intermediate stages or even skip them altogether. In order to test these hypotheses, we plotted multiple proliferating/progenitor signatures into UMAP and found no evidence of overlap in CHIR-treated organoids, thus downplaying the possibility of a prevalent mixed identity. (Supp. Fig 6). Instead, the contour plot and cluster proportions (Fig 6A) pointed to a reduction in the intermediate populations in CHIR treated organoids at day 50 and day100, supporting an accelerated transition though this developmental stage. In order to probe the mechanisms underlying such differences, we harnessed the robustness of gene signatures that define cell cycle phases (S, G2M and G1-G0 by subtraction) from single cell datasets (Tirosh et al., 2016). Under the assumption of homogeneity

for a given cell subpopulation, we could thus estimate the duration of each cycle phase from the number of cells in that particular phase. By this approach we found that indeed the cells in intermediate populations from CHIR-treated organoids have a considerably longer G1 phase at day 100 (Fig. 6B), in agreement with findings from the murine cortex in which a G1 lengthening/S shortening promotes neurogenesis (Calegari, 2005) and consistent with the higher proportion of mature cells found at the same developmental stage (Fig 6A). To further investigate the relations between populations, we used partition-based graph abstraction (PAGA), as a way to quantitatively measure the strength of connectivity across the cells belonging to each cluster, thus inferring functional links among clusters. This approach confirmed a decreased connectivity between clusters 10-2 (Intermediate progenitors) to 4-7-11 (oRG and astrogenic) upon GSK3 inhibition particularly at day100 (Fig 6D) and a global decrease in direct links between the areas corresponding to these subpopulations, which corroborate the finding of an overall reduction of the intermediate-maturity transition.

Finally, by applying pseudotime independently to all conditions and stages, we identified a second developmental trajectory that becomes apparent by day 100 in controls and corresponds to an oRG/astrogenic identity, in agreement with a protracted wave of neurogenesis dependent on oRG production, known to be a feature of primate corticogenesis (Florio and Huttner, 2014, Nowakowski et al., 2016, Bershteyn et al., 2017), (Fig 7A-D). Strikingly, GSK3 inhibition resulted in a severe loss of this oRG/astrogenic trajectory (Fig 7C) and this trajectory was reproduced in the opposite direction by decomposing first and second components (Supp Fig. 8 A-D). Importantly, this finding was independently confirmed by following the developmental evolution based on the oRG-specific marker HOPX, which peaks at day 100 in control organoids (Fig 7A,C), while remaining unchanged in day 100 CHIR- treated organoids compared to day 50 (Fig 7 B,D). Together, these results indicate that GSK3 inhibition results in a severe reduction of oRG population and potentially, oRG-dependent neurogenesis.

Discussion

This work provides the first dissection of the role of GSK3 activity throughout human corticogenesis. As such, it highlights the heuristic power of organoid technology in making human brain development amenable to experimental tractability and functional interrogation. Specifically, our integrated analysis of tissue architecture and transcriptional regulation at single cell resolution uncovers that the activity of GSK3 is essential for cortical morphogenesis but has a surprisingly selective impact on neuronal output, as evidenced by the cell cycle-dependent acceleration of an otherwise uncompromised early neurogenesis vis à vis the dramatic impairment in the emergence and maturation of oRG, a foundational lineage for the specific features of the human cortex.

Role of GSK3 linking morphogenesis and neurogenesis

One of our initially most unexpected findings was the mildness of the defect in early neurogenesis in the face of the massive morphologic disarray of CHIR-treated organoids. This represents possibly the most conspicuous example of a trend that has already begun to emerge in the field of *in vitro* brain organoidogenesis, namely the relative disconnect between tissue morphogenesis and transcriptional identity, since the latter matches frequently with high fidelity the transcriptional milestones of human fetal development even across significant morphological heterogeneity (Camp et al., 2015; Luo et al., 2016; Mariani et al., 2015; Quadrato et al., 2017). Together, these lines of evidence emphasize the resilience and degree of cell-autonomy of the transcriptional programs unfolding during corticogenesis. Indeed, the expression levels of determinants of stage-wise different neuronal maturity determinants (*DCX*, *MAP2*, *MEF2C*, *STMN2*, *TUBB3*) as well as protein levels of the low-layer neuronal progenitor marker TBR1, showed only marginal differences in either direction of dysregulation at day50 and basically no differences at day100 (Fig 3D, Supp Fig 3 B,C). Dissection of single cell populations at day100 allowed to pinpoint localized differences happening in a specific subset of the mature population, differentially affecting the

expression of gene sets including several neuronal fate and function determinants (*BCL11A, PCDH9, GRIA2, MAP2*) (Supp Fig 7) highlighting a surprising specificity for GSK3 impact in fate specification. Depletion of GSK3 activity using pharmacological inhibition or knockdown causes drastic changes in radial glial organization (Yokota et al., 2010). Polarization of radial glia is prerequisite for cortical scaffolding, proper neuronal migration and layering (Shah et al., 2017) and thus alterations of this process results in impaired cortical plate formation (Beattie et al., 2017, Shah et al., 2017). The effects of GSK3 in radial glia polarity constitute fast cellular responses triggered by phosphorylation of targets such as CRMP2, MAP1B and CLASP, which in turn effects modifications and structural changes in microtubule cytoskeleton (Yokota 2010, Hur and Zhou 2010). We did however not observe any differences in expression of canonical polarity markers or determinants of radial glia organization (data not shown), and can therefore conclude that in the human setting GSK3 is not required for the gene expression regulation of polarity determinants per se. Rather, the most salient transcriptional global effect was the upregulation of modulators of cell replication and, in particular, the G2M transition emerged as a recurrent target category among the top enrichments of GSK3-treated samples at all stages (Fig 4H-J), indicating that the modulation of the G2M is a persistent and functionally salient feature of GSK3 activity throughout human corticogenesis.

Several of the known functions of GSK3 characterized in animal models have been recapitulated here, including regulation of neural progenitor proliferation and polarity (Fig 2) and the regulation of neurogenesis (Fig 4) (Hur and Zhou, 2010). Most of these effects have been associated to the modulation of the canonical Wnt pathway and GSEA indeed confirms upregulation of the Wnt gene network conspicuously at day50 and day100 (Fig 4J, supp table 3). However, the lack of causality between effects observed in NSCs and neurogenesis implicates the participation of Wnt-independent mechanisms. Multiple alternative pathways have been shown to mediate GSK3 effects in neurogenesis. For instance, GSK3 induces the release of the scaffold protein axin from membrane compartment and induces its translocation to the nucleus, favoring the production of basal intermediate progenitors in the developing cerebral cortex

(Fang et al., 2013), coherent with our observed decrease in proportion of intermediate progenitors and oRG (Fig 7). Moreover, GSK3 regulates microtubule polarity by targeting MT-linker proteins from the apical junction complexes, (Kumar et al., 2009), which appears as a top downregulated GO category at day 50. From a structural point of view, cell adhesion molecules allow cohesion of neighboring neuroepithelial and apical radial glial cells and are therefore important to maintain the proper tissue architecture (Marthiens et al., 2010). Likewise, conditional deletion of N-cadherin in the mouse cortex leads to AJ disruption, aberrant aRG morphology and polarity, and consequently, to abnormal corticogenesis. Under these conditions, both mitotic and post-mitotic cells were found to be randomly scattered throughout the cortical wall (Kadowaki et al., 2007). It is thus not surprising that even in the absence of an upregulation of Wnt-related gene expression at day 18, the modification of membrane components (Supp Fig 4B) results in changes not only in apical radial glia organization and identity (Zhang et al., 2010).

While we could clearly define populations of postmitotic neurons that are distinguishable among each other on a single cell transcriptome basis, layer or position-based identities were not readily detectable, probably due to the fact that at the stages of differentiation analyzed (day50, day100) the expression levels of known layer-specific transcription factors do not fall within the dynamic range detectable by droplet-based single cell transcriptomics. In this respect, it remains possible that yet deeper coverage may reveal, also at the single cell level, more specific lineage and/or synaptogenic imbalances resulting from CHIR-dependent morphogenetic defects, as hinted by the bulk transcriptome analysis.

GSK3 differentially regulates direct and indirect neurogenic trajectories

During human corticogenesis, most neurons are not generated directly from apical radial glia, but rather indirectly via basal progenitors (BPs) that originate from aRG and are located in the subventricular zone (Bystron et al., 2008; Florio and Huttner, 2014). Depending of the context, depletion of GSK3 may result in either reduced or increased neurogenesis in mice (Kim et al., 2009), indicating that spatiotemporal

regulation of GSK3 activity is required for an appropriate transition from the proliferative to the neurogenic phase occurring during brain development. In human iPSCs, the inhibition of GSK3 during the differentiation into committed neural progenitors favors direct neural induction (Esfandiari et al., 2012). In our chronic setting, starting from a pluripotent state (day0), GSK3 inhibition caused increased proliferation and polarity defects in NCS (Fig 2B-D), which also resulted in larger organoid size (Fig 1A, Fig 3C Supp Fig1) and increased cell numbers in clusters of genetic mature neuronal identity (Fig 6A,B). The dramatic increase in transcriptional impact at day50 compared to day18 (Fig 4), suggests that the early effects in NSCs are magnified in committed and intermediate progenitors, indicating a higher reliance on GSK3 activity at later stages and particularly in IPCs (Ma et al., 2017). In agreement, the population breakdown by single cell analysis revealed a decrease of IPCs and in particular oRGs (Fig 7A) as well as an increase of the duration of their G1 phase, which is well documented to promote neurogenesis by accelerating the entrance in a postmitotic state (Taverna et al., 2014)

The analysis of the pseudotime trajectories in each stage showed the existence of a direct trajectory towards maturity through IPCs at day50, that gets replaced by an indirect trajectory that reaches an oRG/astrogenic identity by day100 (Fig 7A,C). This finding indicates the coexistence of direct and protracted neurogenic trajectories in human cortical organoids. This oRG/astrogenic progeny was significantly depleted in CHIR-treated organoids (Fig 5A) and this was accompanied by a downregulation of several genes of the astrogenic lineage, including SPARCL1 which is upregulated in early astrogenesis and involved in astrocyte-mediated synapse formation (Sloan et al., 2017; Zhang et al., 2016) (Supp Fig 7, B.C)

The disappearance of the indirect neurogenic trajectory at day100 upon CHIR treatment points to a major role of GSK3 in the establishment of IP/oRG populations and hence in oRG-dependent neurogenesis (Fig 7 B,D). Our results indicate that in humans GSK3 role is context-specific, as its inhibition promotes an early oRG-independent neurogenic wave, while impairing oRG-dependent neurogenesis. Finally, the

analysis of population connectivity by PAGA suggested the existence of a previously undescribed link connecting oRG to a newly described early astrogenic branch (Fig 6D), which contains many early astrogenic markers (Fig 5B) although it interestingly lacks the expression of GFAP at this stage (data not shown). The extent to which this new developmental link emerging from *in vitro* organoidogenesis reflects a physiological oRG-astrogenic path in humans should be the subject of future research.

Author contributions

Organoid differentiation and sample collection for the different experiments was done by ALT, ST, NC, ML and BMC. CEV and CC performed bioinformatic analysis. ALT, ST and NC performed single cell experimental procedures. ALT and ML performed organoid stainings and growth curve, ALT performed quantifications and statistical analysis. PC, RC and EC neural induction experiments in 2D. MTR performed proliferation assay in 2D. ALT wrote and the manuscript with contributions from all the authors. GT conceived, designed and supervised the study.

Acknowledgements

This work was supported by the Associazione Italiana per la Ricerca sul Cancro (AIRC) (IG 2014-2018 to G.T.); EPIGEN Flagship Project of the Italian National Research Council (CNR) (to G.T., S.P. and M.P.); the European Research Council (DISEASEAVATARS to G.T.); Fondazione Cariplo (grant 2017-0886 to A.L.T.); Fondazione Italiana per la Ricerca sul Cancro (FIRC) (to P.L.R.); the AIRC grant n° IG2016-ID18575 (to M.P.) and the ERC Consolidator Grant n° 617978 (to M.P.) We are grateful to Pierre-Luc Germain for providing scripts that facilitated this work. We thank Federica Pisati from tissue processing facility.

References

Aberle, H., Bauer, A., Stappert, J., Kispert, A. and Kemler, R. (1997). β-catenin is a target for the ubiquitin-proteasome pathway. *EMBO J.*

Adamo, A., Atashpaz, S., Germain, P.-L., Zanella, M., D'Agostino, G., Albertin, V., Chenoweth, J., Micale, L., Fusco, C., Unger, C., et al. (2015). 7q11.23 dosage-dependent dysregulation in human pluripotent stem cells affects transcriptional programs in disease-relevant lineages TL - 47. *Nat. Genet.* **47 VN-r**, 132–41.

Backman, M., Machon, O., Mygland, L., Van Den Bout, C. J., Zhong, W., Taketo, M. M. and Krauss, S. (2005). Effects of canonical Wnt signaling on dorso-ventral specification of the mouse telencephalon. *Dev. Biol.*

Bagley, J. A., Reumann, D., Bian, S., Lévi-Strauss, J. and Knoblich, J. A. (2017). Fused cerebral organoids model interactions between brain regions. *Nat. Methods* **14**, 743–751.

Beattie, R., Postiglione, M. P., Burnett, L. E., Laukoter, S., Streicher, C., Pauler, F. M., Xiao, G., Klezovitch, O., Vasioukhin, V., Ghashghaei, T. H., et al. (2017). Mosaic Analysis with Double Markers Reveals Distinct Sequential Functions of Lgl1 in Neural Stem Cells. *Neuron*.

Bershteyn, M., Nowakowski, T. J., Pollen, A. A., Di Lullo, E., Nene, A., Wynshaw-Boris, A. and Kriegstein, A. R. (2017). Human iPSC-Derived Cerebral Organoids Model Cellular Features of Lissencephaly and Reveal Prolonged Mitosis of Outer Radial Glia. *Cell Stem Cell* **20**, 435–449.e4.

Betizeau, M., Cortay, V., Patti, D., Pfister, S., Gautier, E., Bellemin-Ménard, A., Afanassieff, M., Huissoud, C., Douglas, R. J., Kennedy, H., et al. (2013). Precursor Diversity and Complexity of Lineage Relationships in the Outer Subventricular Zone of the Primate. *Neuron*.

Birey, F., Andersen, J., Makinson, C. D., Islam, S., Wei, W., Huber, N., Fan, H. C., Metzler, K. R. C., Panagiotakos, G., Thom, N., et al. (2017). Assembly of functionally integrated human forebrain spheroids. *Nature* **545**, 54–59.

Calegari, F. (2005). Selective Lengthening of the Cell Cycle in the Neurogenic Subpopulation of Neural

Progenitor Cells during Mouse Brain Development. *J. Neurosci.*

Camp, J. G., Badsha, F., Florio, M., Kanton, S., Gerber, T., Wilsch-Bräuninger, M., Lewitus, E., Sykes, A., Hevers, W., Lancaster, M., et al. (2015). Human cerebral organoids recapitulate gene expression programs of fetal neocortex development. *Proc. Natl. Acad. Sci.* 201520760.

Chenn, A. and Walsh, C. A. (2003). Increased neuronal production, enlarged forebrains and cytoarchitectural distortions in β-catenin overexpressing transgenic mice. *Cereb. Cortex*.

Coifman, R. R., Lafon, S., Lee, A. B., Maggioni, M., Nadler, B., Warner, F. and Zucker, S. W. (2005). Geometric diffusions as a tool for harmonic analysis and structure definition of data: Multiscale methods. *Proc. Natl. Acad. Sci.*

Conforti, P., Besusso, D., Bocchi, V. D., Faedo, A., Cesana, E., Rossetti, G., Ranzani, V., Svendsen, C. N., Thompson, L. M., Toselli, M., et al. (2018). Faulty neuronal determination and cell polarization are reverted by modulating HD early phenotypes. *Proc. Natl. Acad. Sci.* **115**, E762–E771.

Di Lullo, E. and Kriegstein, A. R. (2017). The use of brain organoids to investigate neural development and disease. *Nat. Rev. Neurosci.* **18**, 573–584.

Eiraku, M., Watanabe, K., Matsuo-Takasaki, M., Kawada, M., Yonemura, S., Matsumura, M., Wataya, T., Nishiyama, A., Muguruma, K. and Sasai, Y. (2008). Self-Organized Formation of Polarized Cortical Tissues from ESCs and Its Active Manipulation by Extrinsic Signals. *Cell Stem Cell* **3**, 519–532.

Esfandiari, F., Fathi, A., Gourabi, H., Kiani, S., Nemati, S. and Baharvand, H. (2012). Glycogen synthase kinase-3 inhibition promotes proliferation and neuronal differentiation of human-induced pluripotent stem cell-derived neural progenitors. *Stem Cells Dev.* **21**, 3233–43.

Florio, M. and Huttner, W. B. (2014). Neural progenitors, neurogenesis and the evolution of the neocortex. *Development* **141**, 2182–2194.

Fumoto, K., Lee, P. C., Saya, H. and Kikuchi, A. (2008). AIP regulates stability of Aurora-A at early mitotic phase coordinately with GSK-3β. *Oncogene*.

González, F., Zhu, Z., Shi, Z. D., Lelli, K., Verma, N., Li, Q. V. and Huangfu, D. (2014). An iCRISPR platform for rapid, multiplexable, and inducible genome editing in human pluripotent stem cells. *Cell Stem Cell*.

Grimes, C. A. and Jope, R. S. (2001a). Creb DNA binding activity is inhibited by glycogen synthase kinase-3?? and facilitated by lithium. *J. Neurochem.*

Grimes, C. A. and Jope, R. S. (2001b). The multifaceted roles of glycogen synthase kinase 3β in cellular signaling. *Prog. Neurobiol.*

Haghverdi, L., Büttner, M., Wolf, F. A., Buettner, F. and Theis, F. J. (2016). Diffusion pseudotime robustly reconstructs lineage branching. *Nat. Methods*.

Harrison-Uy, S. J. and Pleasure, S. J. (2012). Wnt signaling and forebrain development. *Cold Spring Harb. Perspect. Biol.*

Hirabayashi, Y., Itoh, Y., Tabata, H., Nakajima, K., Akiyama, T., Masuyama, N. and Gotoh, Y. (2004). The Wnt/beta-catenin pathway directs neuronal differentiation of cortical neural precursor cells. *Development* **131**, 2791–801.

Hoeflich, K. P., Luo, J., Rubie, E. A., Tsao, M. S., Jin, O. and Woodgett, J. R. (2000). Requirement for glycogen synthase kinase-3β in cell survival and NF-κB activation. *Nature*.

Holland, J. D., Klaus, A., Garratt, A. N. and Birchmeier, W. (2013). Wnt signaling in stem and cancer stem cells. *Curr. Opin. Cell Biol.*

Hur, E. M. and Zhou, F. Q. (2010). GSK3 signalling in neural development. *Nat. Rev. Neurosci.*

Johansson, P. A., Cappello, S. and Götz, M. (2010). Stem cells niches during development-lessons from the cerebral cortex. *Curr. Opin. Neurobiol.*

Kadoshima, T., Sakaguchi, H., Nakano, T., Soen, M., Ando, S., Eiraku, M. and Sasai, Y. (2013). Self-organization of axial polarity, inside-out layer pattern, and species-specific progenitor dynamics in human ES cell-derived neocortex. *Proc. Natl. Acad. Sci.* **110**, 20284–20289.

Kim, W. Y., Wang, X., Wu, Y., Doble, B. W., Patel, S., Woodgett, J. R. and Snider, W. D. (2009). GSK-3 is a master regulator of neural progenitor homeostasis. *Nat. Neurosci.*

Kowalczyk, M. S., Tirosh, I., Heckl, D., Rao, T. N., Dixit, A., Haas, B. J., Schneider, R. K., Wagers, A. J., Ebert, B. L. and Regev, A. (2015). Single-cell RNA-seq reveals changes in cell cycle and differentiation programs upon aging of hematopoietic stem cells. *Genome Res.*

Kuwahara, A., Hirabayashi, Y., Knoepfler, P. S., Taketo, M. M., Sakai, J., Kodama, T. and Gotoh, Y. (2010). Wnt signaling and its downstream target N-myc regulate basal progenitors in the developing neocortex. *Development* **137**, 1035–44.

La Manno, G., Soldatov, R., Zeisel, A., Braun, E., Hochgerner, H., Petukhov, V., Lidschreiber, K., Kastriti, M. E., Lönnerberg, P., Furlan, A., et al. (2018). RNA velocity of single cells. *Nature.*

Lancaster, M. A., Renner, M., Martin, C. A., Wenzel, D., Bicknell, L. S., Hurles, M. E., Homfray, T., Penninger, J. M., Jackson, A. P. and Knoblich, J. A. (2013). Cerebral organoids model human brain development and microcephaly. *Nature* **501**, 373–379.

Lehtinen, M. K., Zappaterra, M. W., Chen, X., Yang, Y. J., Hill, A. D., Lun, M., Maynard, T., Gonzalez, D., Kim, S., Ye, P., et al. (2011). The Cerebrospinal Fluid Provides a Proliferative Niche for Neural Progenitor Cells. *Neuron*.

Liberzon, A., Birger, C., Thorvaldsdóttir, H., Ghandi, M., Mesirov, J. P. and Tamayo, P. (2015). The Molecular Signatures Database Hallmark Gene Set Collection. *Cell Syst.*

Luo, C., Lancaster, M. A., Castanon, R., Nery, J. R., Knoblich, J. A. and Ecker, J. R. (2016). Cerebral Organoids Recapitulate Epigenomic Signatures of the Human Fetal Brain. *Cell Rep.* **17**, 3369–3384.

Ma, Y. C., Song, M. R., Park, J. P., Henry Ho, H. Y., Hu, L., Kurtev, M. V., Zieg, J., Ma, Q., Pfaff, S. L. and Greenberg, M. E. (2008). Regulation of Motor Neuron Specification by Phosphorylation of Neurogenin 2. *Neuron*.

Ma, Y., Wang, X., Chen, J., Li, B., Hur, E.-M. and Saijilafu (2017). Differential Roles of Glycogen Synthase Kinase 3 Subtypes Alpha and Beta in Cortical Development. *Front. Mol. Neurosci.*

Mariani, J., Coppola, G., Zhang, P., Abyzov, A., Provini, L., Tomasini, L., Amenduni, M., Szekely, A., Palejev, D., Wilson, M., et al. (2015). FOXG1-Dependent Dysregulation of GABA/Glutamate

Neuron Differentiation in Autism Spectrum Disorders. *Cell* **162**, 375–390.

McCubrey, J. A., Rakus, D., Gizak, A., Steelman, L. S., Abrams, S. L., Lertpiriyapong, K., Fitzgerald, T. L., Yang, L. V., Montalto, G., Cervello, M., et al. (2016). Effects of mutations in Wnt/β-catenin, hedgehog, Notch and PI3K pathways on GSK-3 activity—Diverse effects on cell growth, metabolism and cancer. *Biochim. Biophys. Acta - Mol. Cell Res.*

McMurtrey, R. J. (2016). Analytic Models of Oxygen and Nutrient Diffusion, Metabolism Dynamics, and Architecture Optimization in Three-Dimensional Tissue Constructs with Applications and Insights in Cerebral Organoids. *Tissue Eng. Part C Methods* **22**, 221–249.

Nowakowski, T. J., Pollen, A. A., Sandoval-Espinosa, C. and Kriegstein, A. R. (2016). Transformation of the Radial Glia Scaffold Demarcates Two Stages of Human Cerebral Cortex Development. *Neuron*.

Nowakowski, T. J., Bhaduri, A., Pollen, A. A., Alvarado, B., Mostajo-Radji, M. A., Di Lullo, E., Haeussler, M., Sandoval-Espinosa, C., Liu, S. J., Velmeshev, D., et al. (2017). Spatiotemporal gene expression trajectories reveal developmental hierarchies of the human cortex. *Science (80-.).*

Paşca, A. M., Sloan, S. A., Clarke, L. E., Tian, Y., Makinson, C. D., Huber, N., Kim, C. H., Park, J.-Y., O'Rourke, N. A., Nguyen, K. D., et al. (2015a). Functional cortical neurons and astrocytes from human pluripotent stem cells in 3D culture. *Nat Methods.* **12**, 671–678.

Patro, R., Duggal, G., Love, M. I., Irizarry, R. A. and Kingsford, C. (2017). Salmon provides fast and bias-aware quantification of transcript expression. *Nat. Methods*.

Patsch, C., Challet-Meylan, L., Thoma, E. C., Urich, E., Heckel, T., O'Sullivan, J. F., Grainger, S. J., Kapp, F. G., Sun, L., Christensen, K., et al. (2015). Generation of vascular endothelial and smooth muscle cells from human pluripotent stem cells. *Nat. Cell Biol.*

Qian, X., Nguyen, H. N., Song, M. M., Hadiono, C., Ogden, S. C., Hammack, C., Yao, B., Hamersky, G. R., Jacob, F., Zhong, C., et al. (2016). Brain-Region-Specific Organoids Using Mini-bioreactors for Modeling ZIKV Exposure. *Cell* **165**, 1238–1254.

Quadrato, G., Nguyen, T., Macosko, E. Z., Sherwood, J. L., Yang, S. M., Berger, D. R., Maria, N., Scholvin, J., Goldman, M., Kinney, J. P., et al. (2017). Cell diversity and network dynamics in photosensitive human brain organoids. *Nature* **545**, 48–53.

Robinson, M. D., McCarthy, D. J. and Smyth, G. K. (2009). edgeR: A Bioconductor package for differential expression analysis of digital gene expression data. *Bioinformatics*.

Setty, M., Tadmor, M. D., Reich-Zeliger, S., Angel, O., Salame, T. M., Kathail, P., Choi, K., Bendall, S., Friedman, N. and Pe'Er, D. (2016). Wishbone identifies bifurcating developmental trajectories from single-cell data. *Nat. Biotechnol.*

Shah, B., Lutter, D., Tsytsyura, Y., Glyvuk, N., Sakakibara, A., Klingauf, J. and Püschel, A. W. (2017). Rap1 GTPases Are Master Regulators of Neural Cell Polarity in the Developing Neocortex. *Cereb. Cortex*.

Šubelj, L. and Bajec, M. (2011). Unfolding communities in large complex networks: Combining defensive and offensive label propagation for core extraction. *Phys. Rev. E - Stat. Nonlinear, Soft Matter Phys.*

Taverna, E., Götz, M. and Huttner, W. B. (2014). The Cell Biology of Neurogenesis: Toward an Understanding of the Development and Evolution of the Neocortex. *Annu. Rev. Cell Dev. Biol.*

Telley, L., Govindan, S., Prados, J., Stevant, I., Nef, S., Dermitzakis, E., Dayer, A. and Jabaudon, D. (2016). Sequential transcriptional waves direct the differentiation of newborn neurons in the mouse neocortex. *Science (80-.).*

Tirosh, I., Izar, B., Prakadan, S. M., Wadsworth, M. H., Treacy, D., Trombetta, J. J., Rotem, A., Rodman, C., Lian, C., Murphy, G., et al. (2016). Dissecting the multicellular ecosystem of metastatic melanoma by single-cell RNA-seq. *Science (80-.).*

Watanabe, K., Kamiya, D., Nishiyama, A., Katayama, T., Nozaki, S., Kawasaki, H., Watanabe, Y., Mizuseki, K. and Sasai, Y. (2005). Directed differentiation of telencephalic precursors from embryonic stem cells. *Nat. Neurosci.* **8**, 288–296.

Wolf, F. A., Angerer, P. and Theis, F. J. (2018). SCANPY: Large-scale single-cell gene expression data analysis. *Genome Biol.*

Yang, Y., Kim, A. H., Yamada, T., Wu, B., Bilimoria, P. M., Ikeuchi, Y., De La Iglesia, N., Shen, J. and Bonni, A. (2009). A Cdc20-APC ubiquitin signaling pathway regulates presynaptic differentiation. *Science (80-.).*

Yokota, Y., Eom, T.-Y., Stanco, A., Kim, W.-Y., Rao, S., Snider, W. D. and Anton, E. S. (2010). Cdc42 and Gsk3 modulate the dynamics of radial glial growth, inter-radial glial interactions and polarity in the developing cerebral cortex. *Development*.

Zheng, G. X. Y., Terry, J. M., Belgrader, P., Ryvkin, P., Bent, Z. W., Wilson, R., Ziraldo, S. B., Wheeler, T. D., McDermott, G. P., Zhu, J., et al. (2017). Massively parallel digital transcriptional profiling of single cells. *Nat. Commun.* **8**, 14049.

Zhou, F. Q., Zhou, J., Dedhar, S., Wu, Y. H. and Snider, W. D. (2004). NGF-induced axon growth is mediated by localized inactivation of GSK-3β and functions of the microtubule plus end binding protein APC. *Neuron*.

Figure legends

Figure 1. Morphogenetic alterations caused by chronic GSK3 inhibition. A. Representative captions cortical organoids differentiated for 18 days and stained with hematoxylin-eosin (upper - 10x, middle - 20x, lower - 63x magnifications), scale bars 200, 50 and 10 μm respectively. **B.** Representative images from day 18 organoids immunostained with anti-PAX6 (red), anti-Ki67 (green), DAPI (blue), widefield fluorescence images acquisition 20X, scale bar = 50 um. Last column panel: digitally rendered magnifications. **C.** Representative images from day 50 organoids immunostained with anti-PAX6 (red), anti-Nestin (green), DAPI (blue), widefield fluorescence images acquisition 20X, scale bar = 50 um. **D** and **E.** Quantification of the proportion of PAX6+ nuclei relative to total nuclei (DAPI). Quantifications were performed in 5

organoids per line, 3 independent hPSC lines (N = 15, n = 3), unpaired t-test *p<0.05, **p<0.01 and ***p<0.001, bars = mean + SD.

Figure 2. GSK3 inhibition disrupts lumen formation in neural stem cells. A. Experimental design: hPSCs differentiated following two parallel protocols, in 3D (up) cortical organoids or 2D (down) dual-smad inhibition. In both cases, parallel rounds were either exposed or not to GSK3 inhibitor CHI99021 (1 uM) starting from day 0 until indicated sample collection timepoint. **B.** Representative captions from immunostaining performed for anti-Pals1(green)/Hoechst(blue), widefield fluorescence images acquisition 20X, scale bar = 20 um. **C.** Bar-plots represent the average ± st.dev. of 5 independent images for lines/conditions; unpaired t-test **p<0.01, ***p<0.001 and ****p<0.0001, error bars = s.e.m. **D.** Lumen quantification (number and area) was performed by CellProfiler software. **E.** Cell proliferation rate was estimate by luminescence assay measurements every with measurements every 24 hours for 96 hours in triplicate n = 3.

Figure 3. GSK3 inhibition increases size and proliferative cell number in cortical organoids. A. Growth curve performed in organoids differentiated for 40 days. Brightfield captions were taken at days 5, 9, 14, 20, 24, 30, 35, 40. Points represent the average of 4 organoids per line. Size quantifications were performed with a custom FIJI function. **B.** Representative images from day 50 organoids stained with CellTox ® green as a marker of cytotoxicity after 72 hours of grow factor starvation (depletion B27 and growfactors). **C.** Quantification of CellTox ® fluorescence at 0, 24,48 and 72 hours after grow factor starvation. **D.** Representative images from day 18 organoids immunostained with anti-DCX (white), anti-KI67 (green), DAPI (blue), widefield fluorescence images acquisition 20X, scale bar = 50 um. **E.** Quantification of the proportion of KI67+ nuclei relative to total nuclei (DAPI) in day 18 organoids. **F.** Day 50 organoids. Quantifications were performed in 5 organoids per line, 3 independent hPSC lines (N = 15, n = 3), unpaired t-test **p<0.01 and ***p<0.001, bars = mean + SD

Figure 4. Impact of GSK3 inhibition on the transcriptional landscape A. Principal Component Analysis performed on the whole transcriptome of untreated and CHIR-treated brain organoids at three stages of development: day 18, day 50 and day 100. **B-D.** Volcano plots illustrating the differential expression analysis for CHIR treatment at day 18 (B), day 50 (C) and day 100 (D). Results obtained by comparing CHIR-exposed versus unexposed samples are reported for the pool of tested genes as $-\log_{10}$FDR and $\log_2$FC. Genes identified as significantly modulated (FDR < 5% and absolute $\log_2$FC > 1) are shown in green, while those respecting only the FDR threshold are depicted in blue and not significant genes (FDR > 5%) are colored in grey. Gene symbols highlight the top-10 up-regulated and down-regulated genes (ranked according to fold-change) in each stage. **E.** Venn diagram depicting the overlap of modulated genes across developmental stages. **F-G.** Scatterplots representing the relationship of the fold-change induced by GSK3 inhibition at day 50 and day18 (F) or day50 and day100 (G), for the subset of genes tested in both conditions. DEGs shared between the two examined conditions are reported in yellow, while DEGs identified selectively at day 18, 50 or 100 are shown in green, blue or violet respectively. **H-J.** Gene expression profiles for genes sets selected among the ones significantly associated with CHIR treatment by GSEA (H: day 18; I: day 50; J: day 100). Expression levels (as z-score) for the 10 top-ranking genes in the leading edge are visualized for each gene set.

Figure 5. Cortical organoids recapitulate the main features of cortical development. A. UMAP plots. For each sub-panel, cells (represented as dots) are colored according to the expression levels of pair combinations of representative cell type markers. **B.** UMAP plot colored by cluster identity; colored lines depict population areas defined by contrast with markers obtained from human fetal brain dataset (apical progenitors in green, intermediate progenitors in yellow, early maturity in magenta, neural maturity in blue, astrogenesis in cyan). Genes pinpointed as characterizing each area (identified by the comparison of the most specific cluster markers with fetal gene signatures) are reported. **C-D.** Diffusion map representing the developmental trajectory of the system. Cells (dots) are colored according to cluster identity (C) and to pseudotime, from origin in black to terminal state in light yellow. **E.** Velocities inferred by Velocyto

analysis are visualized as arrows on the UMAP, underlying transcriptional future state probabilities in single cells. **F.** Visualization of the expression levels of representative genes along pseudotime.

Figure 6. Effects of GSK3 inhibition at a single cell level in day50 and day100 cortical organoids. A. Contour plot representing the difference in frequency distribution in clusters and pseudotime intervals of treated versus untreated cells at day 50 and day 100. Red depicts values higher in CHIR-treated, while blue values higher in CTL. **B.** Z-score calculated on the expression levels of CXCL14, HTR2C, TPD52L1 and visualized as color-code on the UMAP allows to identify a sub-population of cells as exclusively present in non-treated samples. **C.** Distribution of cells across G1, S, G2/M phases of the cell cycle, divided by treatment and stage, in the following populations: apical progenitors, intermediate progenitors, early maturity, neural maturity, astrogenesis. The mosaic plots report for each population the percentage of cells in each phase (G1:grey; S:green; G2M: purple); percentage are reported for S phase. **D.** PAGA analysis applied stage and treatment-wise on the 15 clusters identified on the complete dataset. Circle diameter represents the fraction of cells assigned to each cluster; edge thickness visualizes the strength of connections across cells of the related clusters.

Figure 7 Unbiased pseudotime trajectories followed by organoid single cell populations at day50 and day100 A-D. Over-imposition of pseudotime analyses performed separately for each experimental condition as color-scale on UMAP calculated on the complete system (as in Fig. 4A). Blue identifies origin; dark red the terminal state. Visualization of the expression levels of representative genes along the condition-specific pseudotime.

Figure 1.

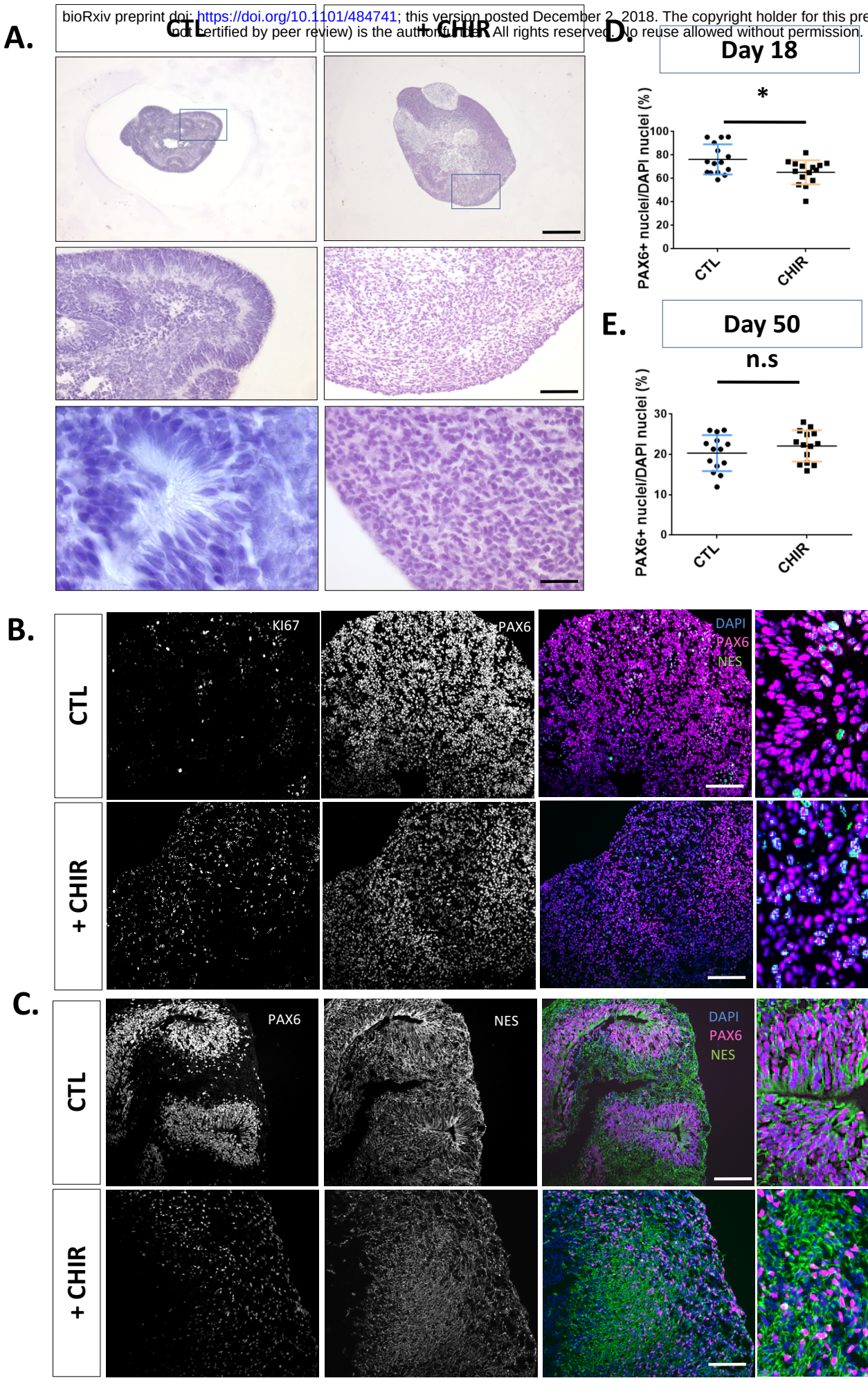

Figure 2.

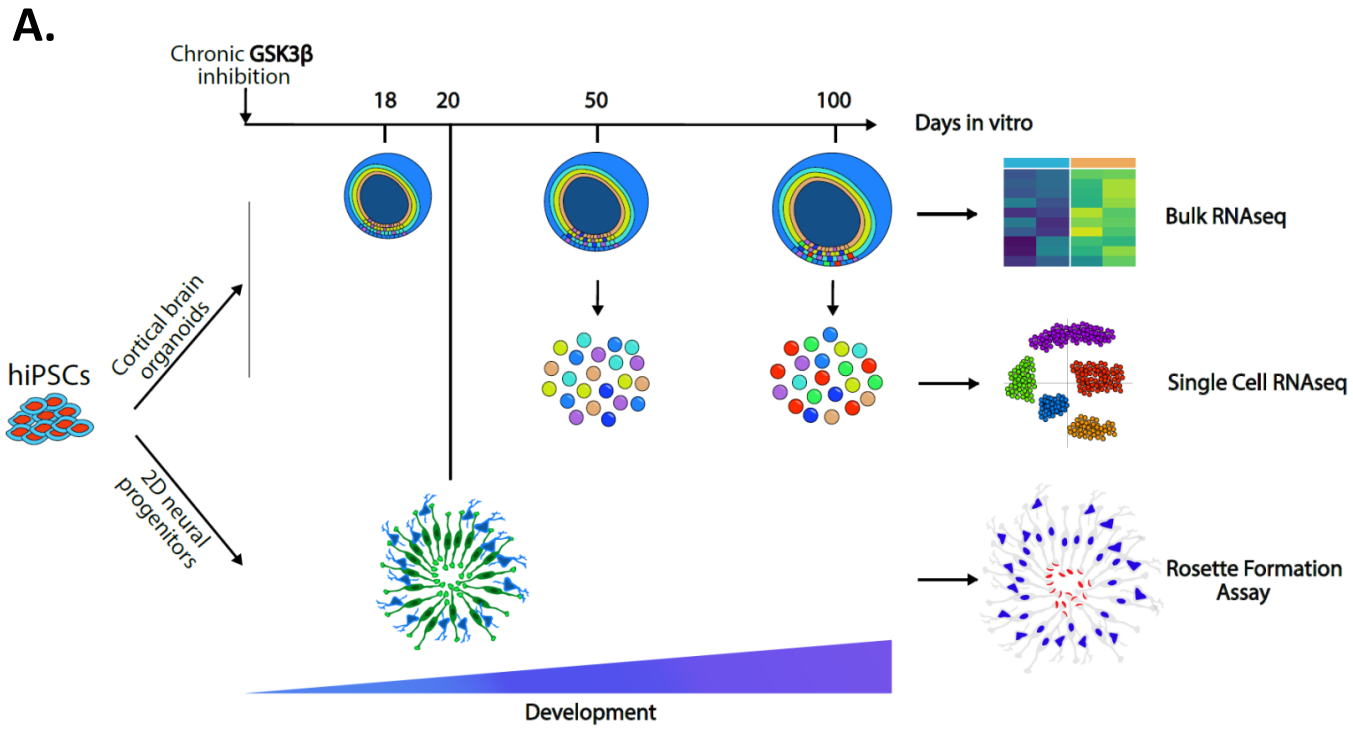
A.
Chronic GSK3β inhibition
18
20
50
100
Days in vitro
hiPSCs
Cortical brain organoids
2D neural progenitors
Bulk RNAseq
Single Cell RNAseq
Rosette Formation Assay
Development

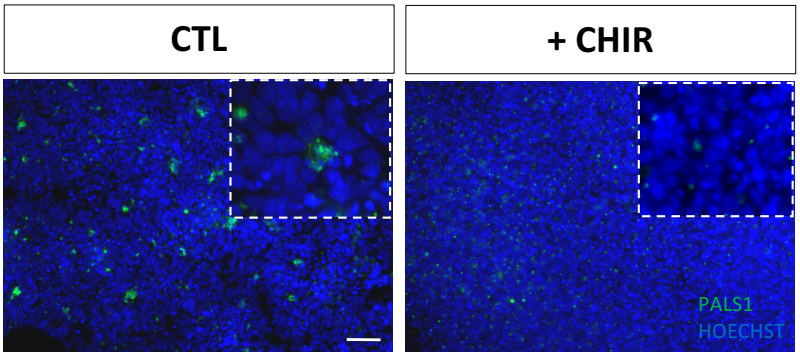
B.
CTL
+ CHIR
PALS1
HOECHST

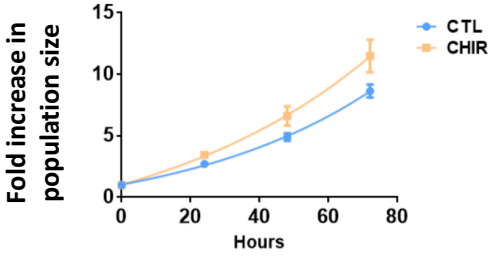
E.
Fold increase in population size
15
10
5
0
0
20
40
60
80
Hours
CTL
CHIR

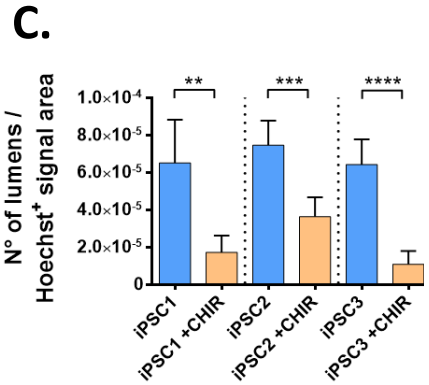
C.
N° of lumens / Hoechst+ signal area
1.0×10-4
8.0×10-5
6.0×10-5
4.0×10-5
2.0×10-5
0
**
***
****
iPSC1
iPSC1 +CHIR
iPSC2
iPSC2 +CHIR
iPSC3
iPSC3 +CHIR

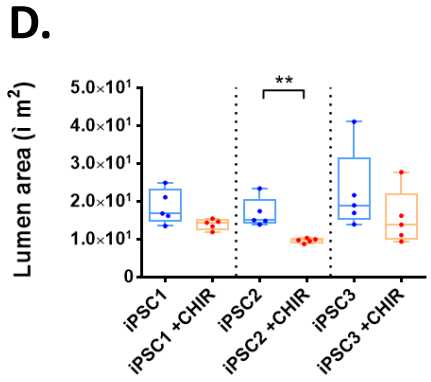
D.
Lumen area (i m2)
5.0×101
4.0×101
3.0×101
2.0×101
1.0×101
0
**
iPSC1
iPSC1 +CHIR
iPSC2
iPSC2 +CHIR
iPSC3
iPSC3 +CHIR

Day

A.

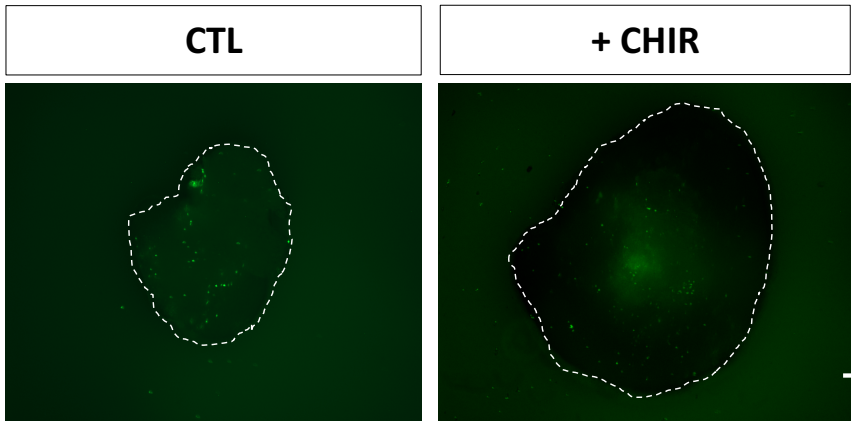

B.

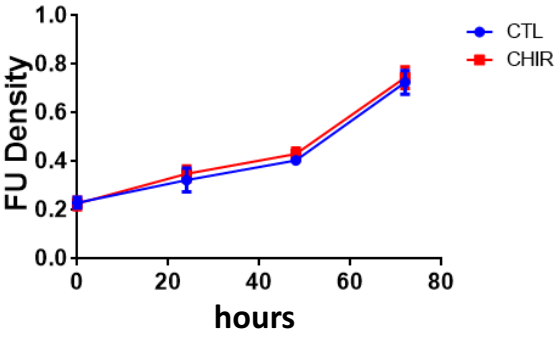

Figure 3.

C.

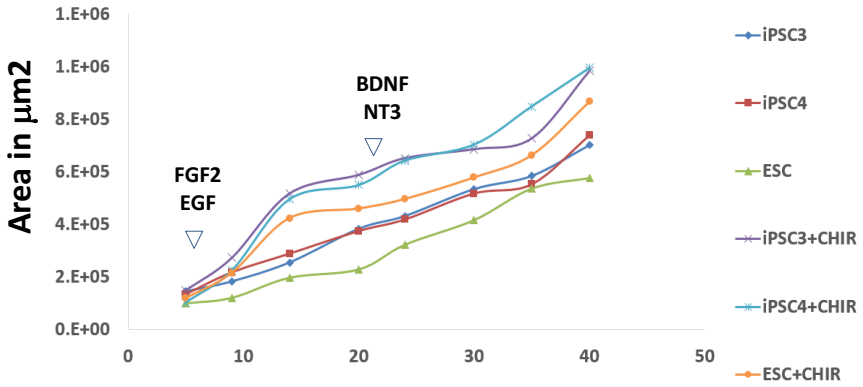

D.

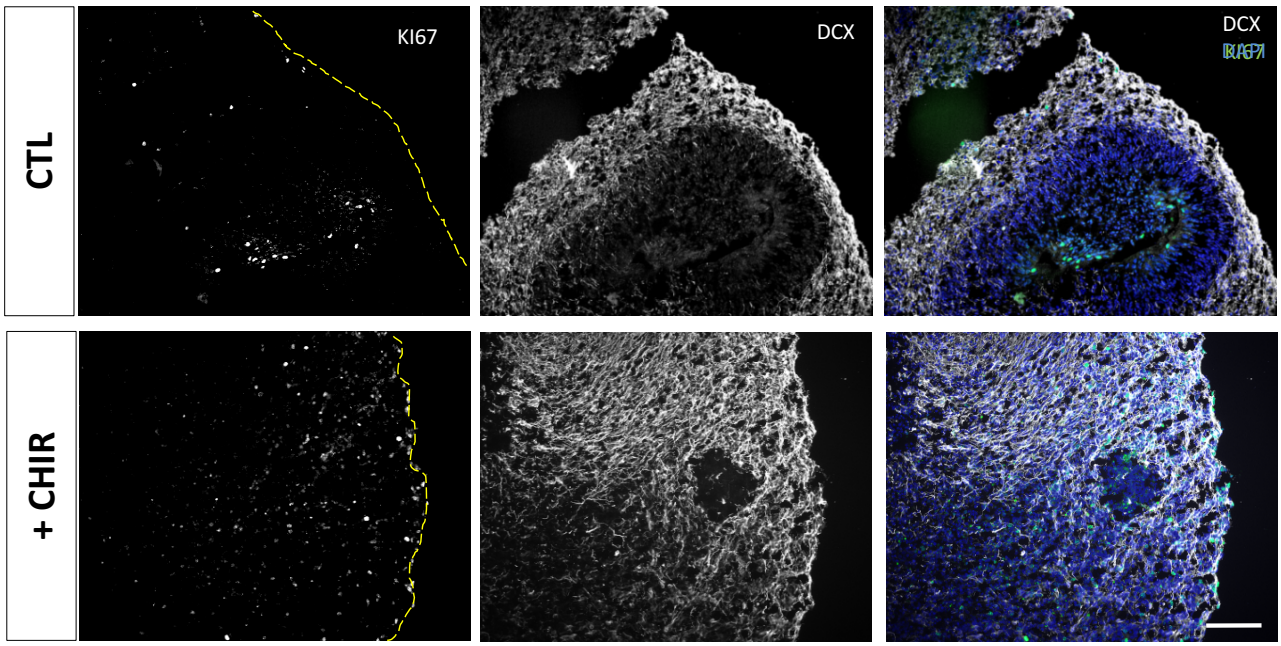

E.

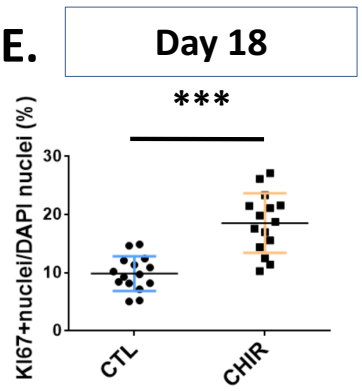

F.

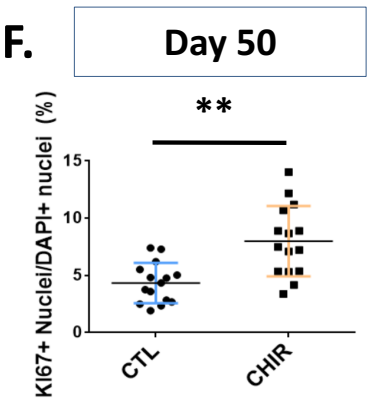

Figure 4.

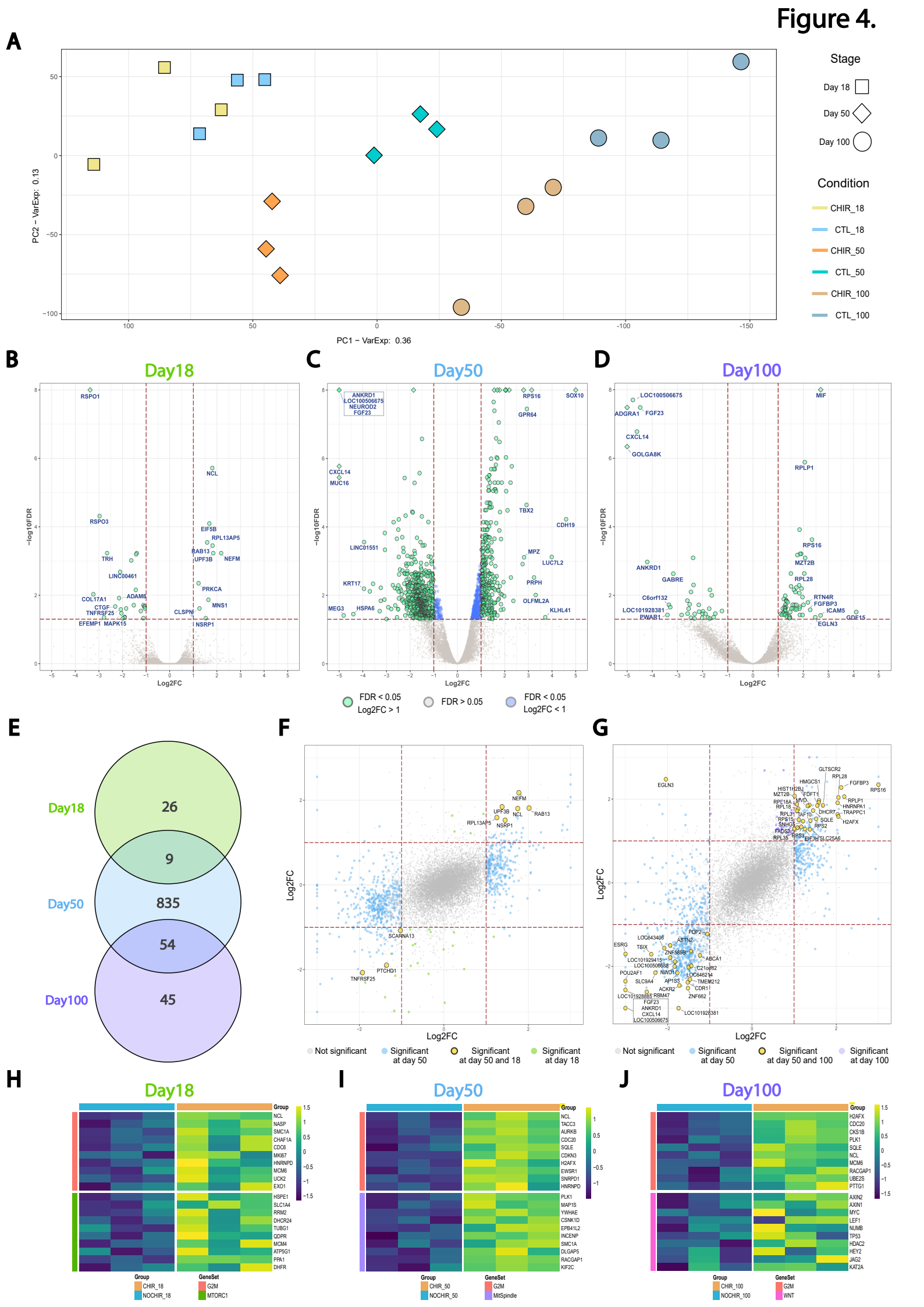
A
PC2 – VarExp: 0.13
PC1 – VarExp: 0.36
Stage
Day 18
Day 50
Day 100
Condition
CHIR_18
CTL_18
CHIR_50
CTL_50
CHIR_100
CTL_100
B
Day18
C
Day50
D
Day100
−log10FDR
Log2FC
FDR < 0.05
Log2FC > 1
FDR > 0.05
FDR < 0.05
Log2FC < 1
E
Day18
Day50
Day100
26
9
835
54
45
F
G
Log2FC
Not significant
Significant at day 50
Significant at day 50 and 18
Significant at day 18
Significant at day 50 and 100
Significant at day 100
H
Day18
I
Day50
J
Day100
Group
GeneSet
CHIR_18
NOCHIR_18
G2M
MTORC1
CHIR_50
NOCHIR_50
MitSpindle
CHIR_100
NOCHIR_100
WNT

Figure 5.

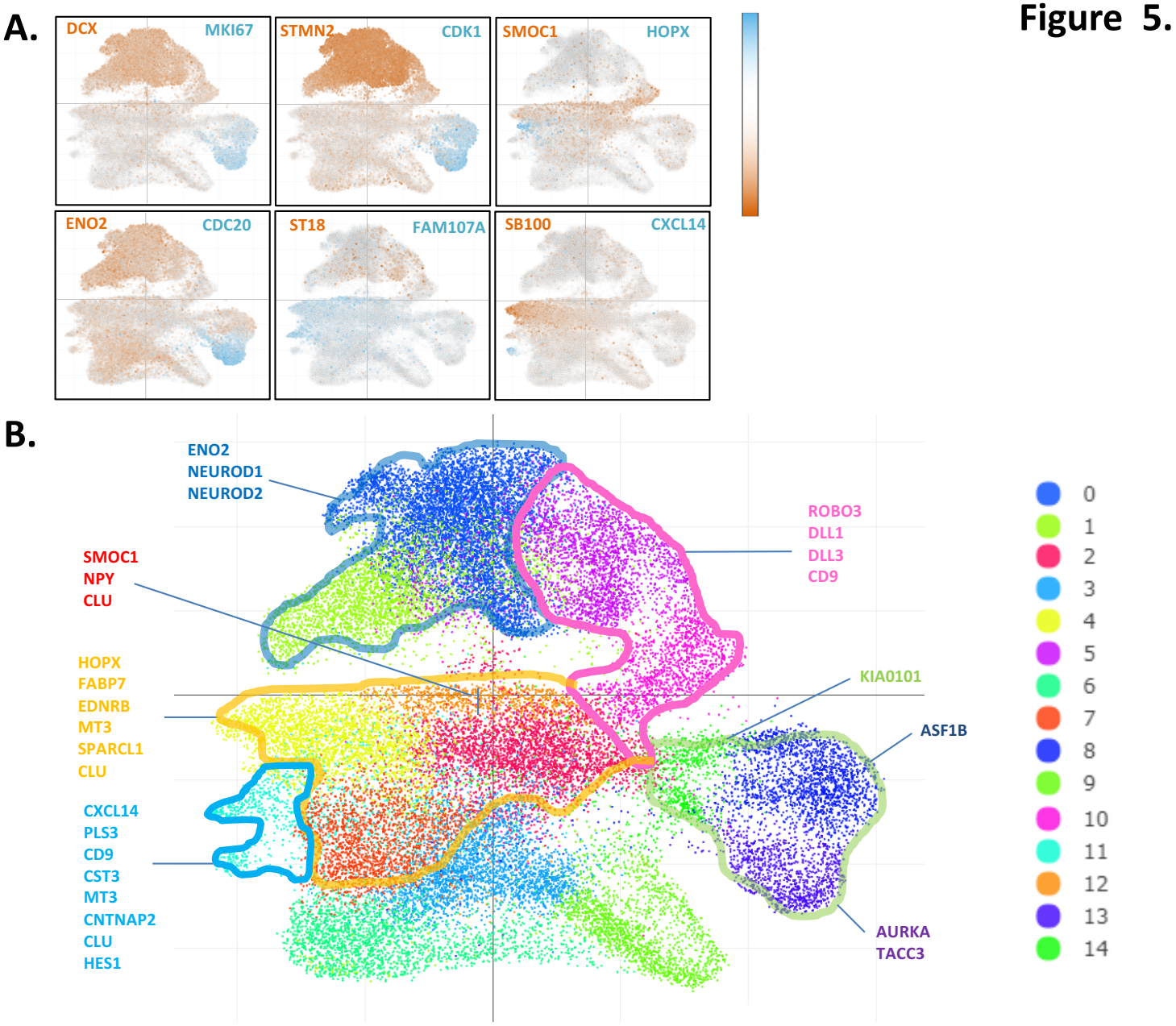
A.
DCX
MKI67
STMN2
CDK1
SMOC1
HOPX
ENO2
CDC20
ST18
FAM107A
SB100
CXCL14
B.
ENO2
NEUROD1
NEUROD2
SMOC1
NPY
CLU
HOPX
FABP7
EDNRB
MT3
SPARCL1
CLU
CXCL14
PLS3
CD9
CST3
MT3
CNTNAP2
CLU
HES1
ROBO3
DLL1
DLL3
CD9
KIA0101
ASF1B
AURKA
TACC3
0
1
2
3
4
5
6
7
8
9
10
11
12
13
14
C.
D.
0.0
0.1
0.2
0.3
0.4
0.5
0.6
0.7
0.8
0.9
1.0
E.
F.
Normalized expression
Wishbone trajectory
MKI67
HOPX
DCX
CDK1
SMOC1
STMN2

Figure 6

A.

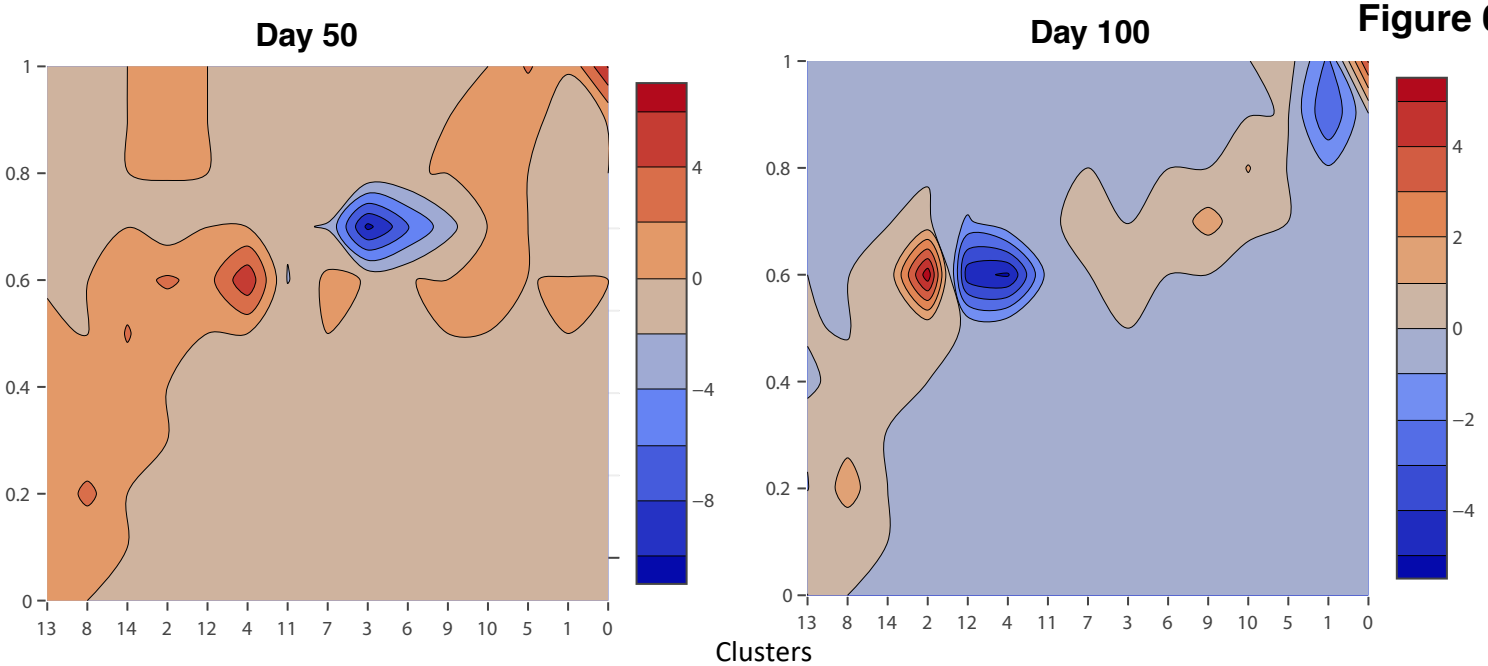

	13	8	14	2	12	4	11	7	3	6	9	10	5	1	0
CTLD50	4%	6%	3%	13%	1%	4%	6%	7%	15%	10%	7%	3%	5%	8%	8%
CHIR50	5%	9%	7%	14%	2%	10%	2%	5%	4%	4%	5%	4%	7%	7%	15%
CTLD100	2%	3%	2%	4%	7%	11%	2%	5%	2%	2%	2%	5%	10%	12%	28%
CHIRD100	4%	6%	3%	10%	2%	6%	2%	5%	2%	3%	3%	6%	10%	6%	32%

B.

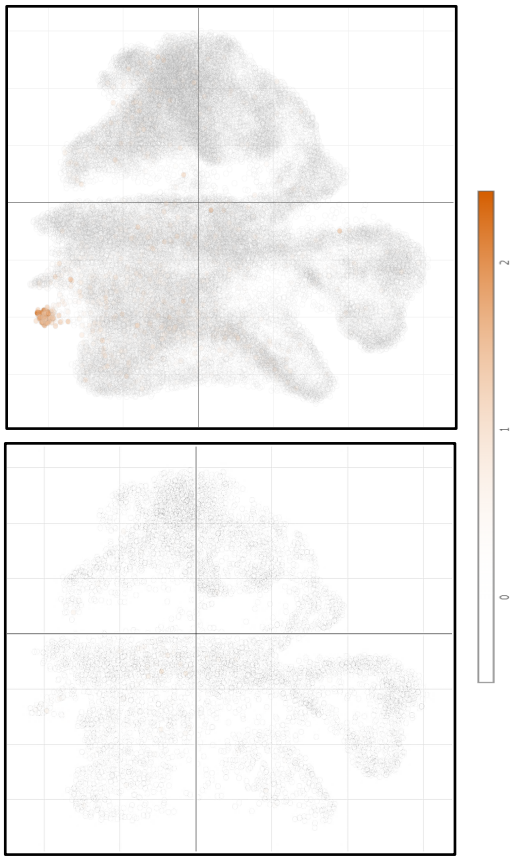

C.

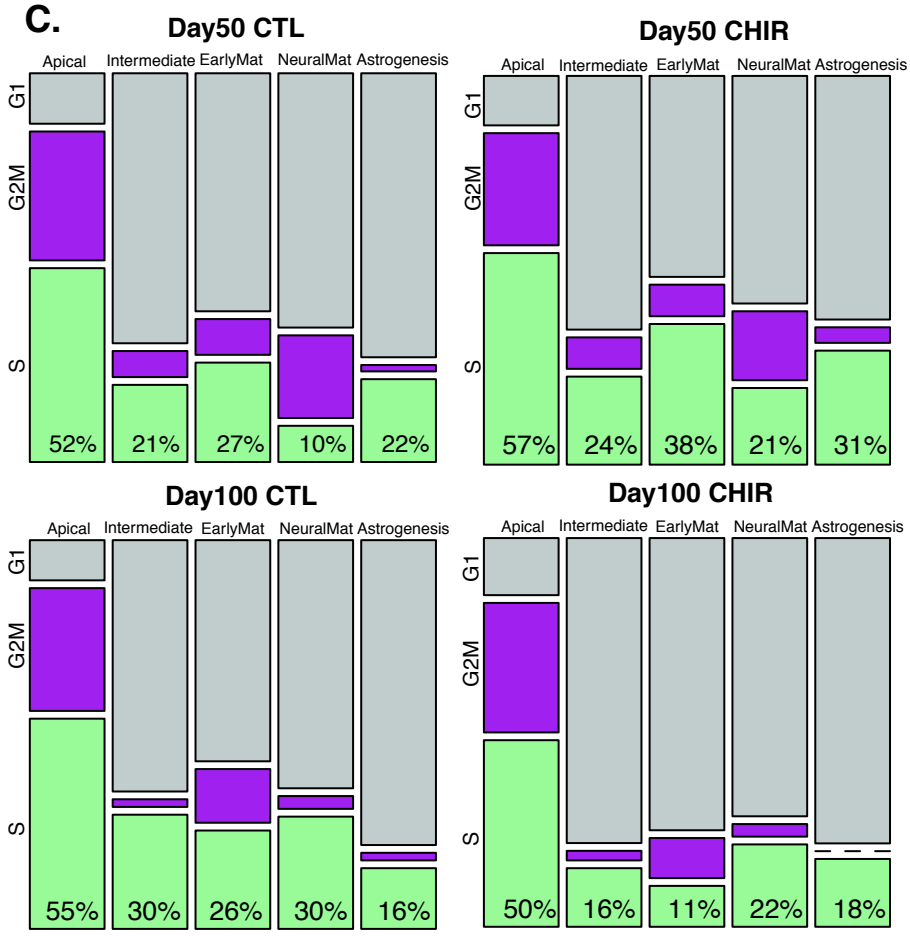

D.

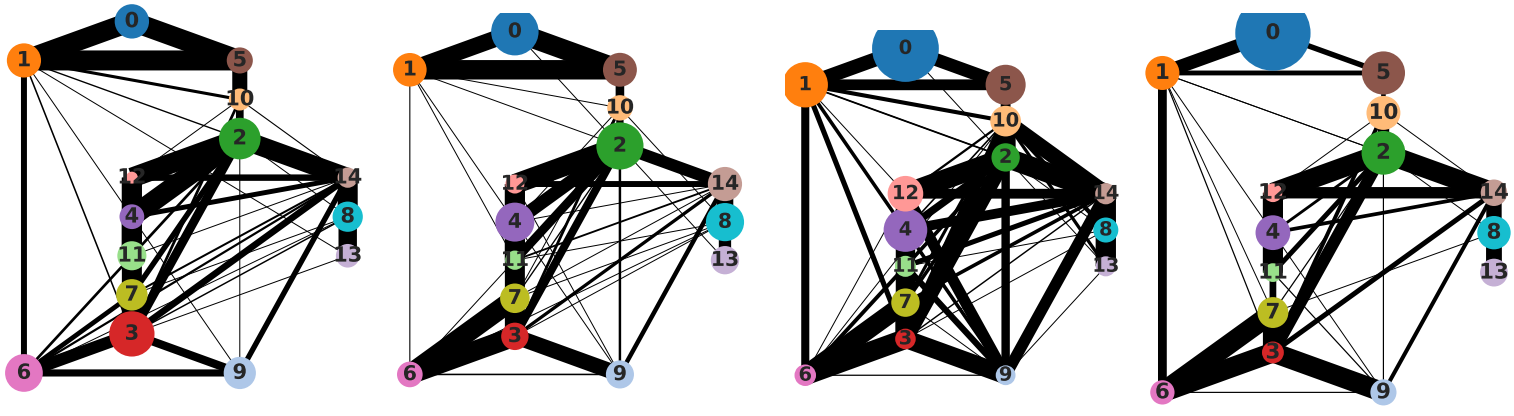

Figure 7.

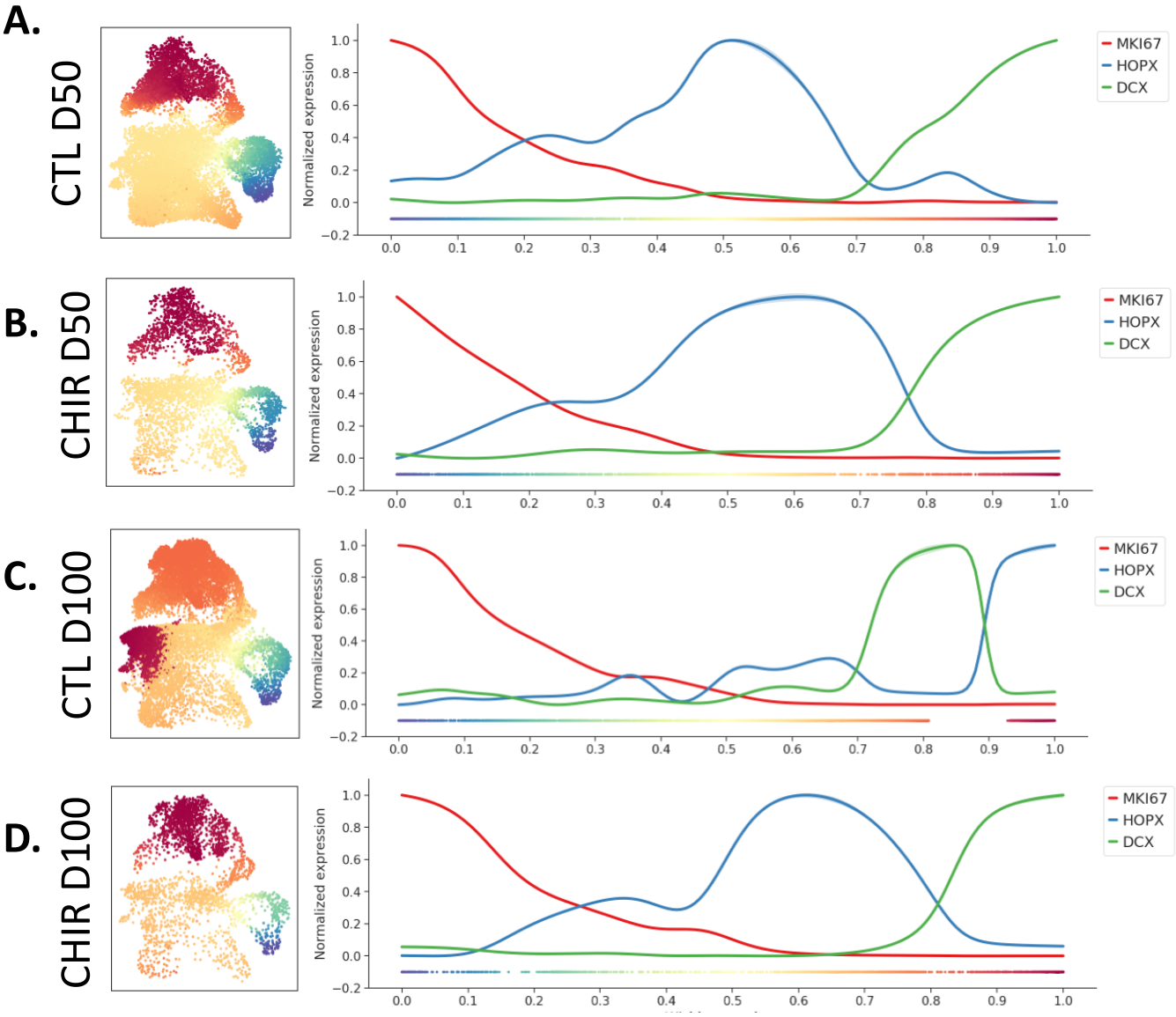
A.
CTL D50
B.
CHIR D50
C.
CTL D100
D.
CHIR D100
Normalized expression
MKI67
HOPX
DCX